

Testing an indirect method for identifying galaxies with high levels of Lyman continuum leakage

Satoshi Yamanaka,^{1,2*} Akio K. Inoue,^{1,2,3} Toru Yamada,⁴ Erik Zackrisson,⁵
Ikuru Iwata,⁶ Genoveva Micheva,⁷ Ken Mawatari,⁸ Takuya Hashimoto^{1,2,6,9}
and Mariko Kubo⁶

¹Waseda Research Institute for Science and Engineering, Faculty of Science and Engineering, Waseda University, 3-4-1, Okubo, Shinjuku, Tokyo 169-8555, Japan

²Department of Environmental Science and Technology, Faculty of Design Technology, Osaka Sangyo University, 3-1-1, Nakagaito, Daito, Osaka 574-8530, Japan

³Department of physics, School of Advanced Science and Engineering, Faculty of Science and Engineering, Waseda University, 3-4-1, Okubo, Shinjuku, Tokyo 169-8555, Japan

⁴Institute of Space and Astronautical Science, Japan Aerospace Exploration Agency, 3-1-1, Yoshinodai, Chuo-ku, Sagami-hara, Kanagawa 252-5210, Japan

⁵Department of Physics and Astronomy, Uppsala University, Box 515, SE-751 20 Uppsala, Sweden

⁶National Astronomical Observatory of Japan, 2-21-1 Osawa, Mitaka, Tokyo 181-8588, Japan

⁷Leibniz-Institut für Astrophysik, An der Sternwarte 16, D-14482 Potsdam, Germany

⁸Institute for Cosmic Ray Research, The University of Tokyo, 5-1-5 Kashiwa-no-Ha, Kashiwa, Chiba 277-8582, Japan

⁹Tomonaga Center for the History of the Universe (TCHoU), Faculty of Pure and Applied Sciences, University of Tsukuba, Tsukuba, Ibaraki 305-8571, Japan

Accepted XXX. Received YYY; in original form ZZZ

ABSTRACT

Using a sample of galaxies at $z \approx 3$ with detected Lyman Continuum (LyC) leakage in the SSA22 field, we attempt to verify a proposed indirect method for identifying cases with high LyC escape fraction f_{esc} based on measurements of the H β equivalent width (EW) and the β slope of the UV continuum. To this end, we present Keck/MOSFIRE H β emission line flux measurements of LyC galaxies (LCGs) at spectroscopic redshifts $z_{\text{spec}} \sim 3.3$, Lyman break galaxies (LBGs) at photometric redshifts $z_{\text{phot}} = 2.7\text{--}3.7$, and Ly α emitters at $z_{\text{phot}} = 3.1$. We also reconfirm the spectroscopic redshifts and measure the H β emission line fluxes from 2 LCGs and 6 LBGs. For the LCG in our sample with the most extreme f_{esc} , as revealed by the direct detection of LyC photons, we find that the EW(H β)– β method gives a broadly consistent estimate for f_{esc} , although the error bars remain very large. We also discuss how a combination of f_{esc} measurements based on direct and indirect methods can shed light on the LyC escape mechanism and the anisotropy of the leakage.

Key words: galaxies: high-redshift – galaxies: starburst – galaxies: ISM

1 INTRODUCTION

Cosmic reionization is a phase transition from the neutral to ionized state of the intergalactic medium (IGM), likely driven by ionizing radiation from star-forming galaxies (SFGs) and/or active galactic nuclei (AGNs; e.g. Madau et al. 1999; Madau & Haardt 2015; Robertson et al. 2015). Various observations indicate that the reionization process was completed by $z \sim 6$: the Gunn–Peterson optical depth (e.g. Fan et al. 2002, 2006), the clustering of Ly α Emitters (LAEs; e.g. Ouchi et al. 2010, 2018), the evolution of the luminosity function of LAEs (e.g. Kashikawa et al. 2006, 2011; Itoh et al. 2018; Konno et al. 2018), the fraction of Ly α emitting galaxies in SFGs (e.g. Ono et al. 2012; Schenker et al. 2012), the Ly α damping wing in gamma-ray burst after-glow spectra (e.g. Totani et al. 2006, 2016; Greiner et al. 2009), and the kinetic Sunyaev–Zeldovich effect (e.g. Zahn et al. 2012; Planck Collaboration et al. 2016). However,

despite a great deal of effort to understand cosmic reionization, the detailed history, sources, and topology of this epoch are not yet understood.

In order to understand the dominant sources of cosmic reionization, the fraction of ionizing photons (Lyman continuum, hereafter LyC, at $\lambda_{\text{rest}} < 912\text{\AA}$) that escapes from SFGs/AGNs into the surrounding IGM, f_{esc} , is one of the most important physical quantities. For reionization by SFGs, a LyC escape fraction on the order of 10% seems to be required (e.g. Inoue et al. 2006; Finkelstein et al. 2015, 2019; Bouwens et al. 2016). Based on current constraints, the contribution from AGNs to the reionization process moreover appears to be subdominant compared to that of SFGs (e.g. Micheva et al. 2017a; Matsuoka et al. 2018; Kulkarni et al. 2019).

The simplest and most robust way to constrain f_{esc} is direct imaging and/or direct spectroscopic observations of the escaping LyC photons. The standard procedure is to estimate f_{esc} of SFGs/AGNs from their observed luminosity ratio of ionizing to non-ionizing ultraviolet (UV) radiation, $L_{\text{UV,obs}}/L_{\text{LyC,obs}}$, using

* E-mail: syamanaka@aoni.waseda.jp

assumptions on the intrinsic luminosity ratio of $L_{\text{UV,int}}/L_{\text{LyC,int}}$, the IGM absorption along its sightline, and the dust attenuation (e.g. Steidel et al. 2001; Inoue et al. 2005; Siana et al. 2007).

Since it is next to impossible to directly observe the LyC photons escaping from SFGs/AGNs at $z > 5$ due to foreground IGM absorption (Inoue & Iwata 2008), the LyC observations for lower- z analogs are important for inferring the likely f_{esc} of SFGs/AGNs in the epoch of cosmic reionization, and to test indirect methods of estimating f_{esc} .

Numerous attempts have been made to estimate the LyC escape fractions of individual SFGs at $z < 4$. Since Earth's atmosphere is very efficient in absorbing far-UV radiation, space telescopes such as the Far Ultraviolet Spectroscopic Explorer (*FUSE*) and the Hubble Space Telescope (*HST*) have very been important for studying the f_{esc} of local and/or low- z SFGs. Several detections of direct LyC radiation from $z < 1$ starburst galaxies have been made, typically with $f_{\text{esc}} \lesssim 10\%$ (e.g. Bergvall et al. 2006; Leitet et al. 2011, 2013; Borthakur et al. 2014; Izotov et al. 2016a,b), although some objects have been reported with $f_{\text{esc}} \sim 40\text{--}70\%$ (Izotov et al. 2018a,b). At $z \approx 2\text{--}4$, the f_{esc} values of SFGs have been investigated by both space and ground based telescopes. In this redshift range, many individual objects appear to show relatively high f_{esc} ($f_{\text{esc}} \gtrsim 10\%$) compared to the local value (e.g. Steidel et al. 2001, 2018; Iwata et al. 2009, 2019; Mostardi et al. 2015; Shapley et al. 2016; Vanzella et al. 2016, 2018; Bian et al. 2017; Micheva et al. 2017b; Naidu et al. 2017; Fletcher et al. 2019).

At the same time, attempts to estimate the *typical* f_{esc} using stacked samples at $z = 1\text{--}3$ indicate that this value may be much lower. These stacking analyses often result in non-detections of LyC, with corresponding upper limits at $f_{\text{esc}} < \text{several } \%$ (e.g. Siana et al. 2007, 2010; Vanzella et al. 2010b; Grazian et al. 2016; Micheva et al. 2017b). A very low typical $f_{\text{esc}} \approx 0.5\%$ has also been derived from the study of gamma-ray bursts at $z \approx 1.6\text{--}6.7$ (Tanvir et al. 2019). Hence, the average f_{esc} at these intermediate redshifts may be on the low side of what would be required for cosmic reionization (but see Finkelstein et al. 2019, for an attempt to explain reionization with $f_{\text{esc}} \leq 5\%$). Whether the average f_{esc} increases as one approaches the epoch of reionization ($z > 6$) remains an open question.

Since studies of individual objects with LyC detections report significant f_{esc} values (from several % at $z \sim 0$ to $10\text{--}60\%$ at $z \sim 3\text{--}4$), it is likely that the LyC escape depends strongly on physical quantities such as the properties of gas and dust in the ISM, the viewing angle, the star formation rate, and/or the stellar mass (e.g. Nestor et al. 2011, 2013; Mostardi et al. 2013). For a statistical discussion, it is important to collect data on LyC-detected SFGs which cover a wide parameter space in terms of physical characteristics. In numerical simulations, less-massive and/or UV fainter SFGs, which are more abundant than massive and/or UV brighter SFGs, are for instance often predicted to have high f_{esc} and hence contribute significantly to cosmic reionization (e.g. Yajima et al. 2011; Wise et al. 2014; Paardekooper et al. 2015).

Depending on the physical mechanism behind the leakage, this can have number of distinct effects on various spectral features. When the escape path is optically thin to Ly α photons ($\tau_{\text{Ly}\alpha} \sim 1$ for $\log N_{\text{HI}} \sim 13$), the escape path is also optically thin to LyC photons ($\tau_{\text{LyC}} \sim 1$ for $\log N_{\text{HI}} \sim 17$). Hence, one expects a positive correlation between f_{esc} and the emission-line equivalent width (EW) of Ly α (e.g. Micheva et al. 2017b; Steidel et al. 2018). When assuming the link of the escape path between LyC and Ly α , the line profile of Ly α also becomes a probe for f_{esc} (Verhamme et al. 2015, 2017; Dijkstra et al. 2016). The luminosity ratio of [O III] $\lambda\lambda 4959, 5007$ and [O II] $\lambda 3727$, [O III]/[O II], has also been suggested as a probe for

high- f_{esc} SFGs (Nakajima et al. 2013; Nakajima & Ouchi 2014). Indeed, very high f_{esc} ($f_{\text{esc}} \gtrsim 50\%$) are found among SFGs with high [O III]/[O II] at both low and high z (de Barros et al. 2016; Vanzella et al. 2016, 2018; Izotov et al. 2018a). Even so, Nakajima et al. (2019) report that no LyC escape is detected for some SFGs despite a high [O III]/[O II] ratio. Hence, it seems that a high [O III]/[O II] ratio may be a necessary, rather than sufficient condition for LyC leakage.

Although there have been attempts to determine f_{esc} for SFGs at $z < 4$ from direct LyC measurements, our knowledge of f_{esc} is still far from complete. There are essentially five difficulties in estimating f_{esc} from direct LyC measurements. First of all, it is hard to directly observe the escaping LyC photons from high- z SFGs (and almost impossible from SFGs at $z > 5$) due to the foreground absorption by H I clouds in the IGM such as Lyman limit systems (e.g. Inoue & Iwata 2008; Inoue et al. 2014). Second, significant sightline-to-sightline variations in IGM absorption are predicted (Inoue & Iwata 2008; Vasei et al. 2016; Steidel et al. 2018), which may be difficult to assess for individual targets. In fact, Rivera-Thorsen et al. (2019) report on large variations among the multiply-imaged LyC spots from a gravitationally lensed SFG at $z = 2.4$. Third, it is possible that the observed flux, which is assumed to be due to escaping LyC photons, does not come from SFGs at high z but from the foreground (low- z) interlopers (Vanzella et al. 2010a; Siana et al. 2015). Fourth, the leakage may be anisotropic, so that the f_{esc} measured in our direction may deviate significantly from the total f_{esc} of the target galaxy. Finally, because the UV light especially at $\lambda_{\text{obs}} \lesssim 3000\text{\AA}$ is absorbed by the Earth's atmosphere, we need space telescopes for the direct LyC measurements of low- z objects. In order to investigate the redshift evolution of f_{esc} and the detailed correlations between f_{esc} and other physical quantities, we would greatly benefit from an indirect method which can avoid these problems.

Zackrisson et al. (2013) have proposed a scheme to indirectly assess f_{esc} from two observational quantities not affected by IGM attenuation – the H β line equivalent width (EW) and the rest-frame intrinsic UV spectral slope β , defined as $f_{\lambda} \propto \lambda^{\beta}$ at $\lambda_{\text{rest}} \sim 1300\text{--}2500\text{\AA}$ (Calzetti et al. 1994). This EW(H β)- β method is based on the simple idea that a high fraction of LyC photons absorbed in H II regions of SFGs should result in stronger nebular emission and a larger EW(H β). The equivalent width of nebular emission also depends on the production rate of LyC photons, but the UV spectral slope β can potentially be used to gauge this, as a blue UV slope is expected to go hand in hand with a high production rate. As a consequence, the distribution of SFGs across the EW(H β)- β diagram could make it possible to single out high- f_{esc} cases.

This method was designed for identifying extreme cases of LyC leakage in the $z > 6$ galaxy population, which are out of reach of direct LyC detection methods, and originally based on simple toy models for such galaxies. However, Zackrisson et al. (2017) also show the validity of this idea for SFGs at $z > 6$ in cosmological simulations. If verified, this could be a useful tool for studying LyC leakage with the James Webb Space Telescope (*JWST*), which will be able to spectroscopically detect H β in large samples of galaxies up to $z \approx 9$.

However, before attempting to apply the EW(H β)- β method to SFGs at $z > 6$, it would be very useful to verify this method with SFGs for which the LyC has been measured through direct means, so that the f_{esc} derived from the direct and indirect methods can be compared. This requires applying the method to galaxies at $z < 4$, and comes with a number of challenges. Observations have revealed that there is a trend in β with redshift in the sense that

reionization-epoch galaxies tend to have bluer UV slopes (Bouwens et al. 2014), likely due to evolution in both dust attenuation and stellar population age (Wilkins et al. 2013). Without recalibrating the method to simulations at $z < 6$, it is therefore necessary to identify a suitable lower-redshift analog with properties that match the $z > 6$ galaxy population as closely as possible. The ideal case would be to detect high levels of LyC from a galaxy with a very blue UV slope, indicative of low dust reddening, although the exact β limit for this depends on $\text{EW}(\text{H}\beta)$ as well. The comparison may also be compromised due to the way anisotropic leakage and uncertainties in the IGM line-of-sight absorption may affect the direct f_{esc} measurement. Despite these difficulties, we here set out to attempt this test, starting from a sample of $z \approx 3$ galaxies in the SSA22 field.

In this paper, we present results of our K -band spectroscopic measurements of the $\text{H}\beta$ emission line flux from Lyman Continuum Galaxies (hereafter LCGs), which are SFGs with direct LyC detections at $z \sim 3.3$, as well as Lyman break galaxies (LBGs) and LAEs in the SSA22 field. In the end, we are able to identify one very blue LCG for which the $\text{EW}(\text{H}\beta)$ - β method may be applied without modifications, and find that the f_{esc} estimated from this technique is broadly consistent with f_{esc} derived from the direct LyC measurement. Stronger constraints (and hence a more decisive test) would, however, require a significant reduction of the observational errors on both $\text{EW}(\text{H}\beta)$ and β .

In section 2, we describe the details of our sample of LCGs/LBGs/LAEs. In section 3, we describe the spectroscopic observations and the data reductions. In section 4, we explain the method used for measuring the UV spectral slope β , the emission line flux, and $\text{EW}(\text{H}\beta)$. In section 5, we show our main result, i.e., the $\text{EW}(\text{H}\beta)$ - β diagram. In section 6, we discuss the $\text{EW}(\text{H}\beta)$ - β method in comparison to the direct LyC measurement. Our results are summarized in section 7. In regard to the cosmological parameters, we assume $\Omega_{m,0} = 0.3$, $\Omega_{\Lambda,0} = 0.7$, $H_0 = 70 \text{ km s}^{-1} \text{ Mpc}^{-1}$. Throughout this work, we adopt the AB magnitude system (Oke & Gunn 1983; Fukugita et al. 1996).

2 SAMPLE

2.1 Photometric catalog

In this work, we use the SSA22 H I Tomography (SSA22HIT) master catalog (Mawatari et al. in preparation). The purpose of the SSA22HIT project is to reveal the spatial distribution of H I gas in the SSA22 proto-cluster field through the use of Ly α forest tomography (Lee et al. 2014, 2018). For this purpose, they compile the photometry of available broad-band and narrow-band filters in the SSA22 field, and make a catalog of LAEs and LBGs in a range of photometric redshift ($z_{\text{phot}} = 2.7\text{--}3.7$). The catalog includes the photometry of broad-band and narrow-band filters of the Canada-France-Hawaii Telescope (CFHT)/MegaCam (Boulade et al. 2003), Subaru/Suprime-Cam (Scam; Miyazaki et al. 2002), Subaru/Hyper Suprime-Cam (HSC; Miyazaki et al. 2012, 2018), Subaru/MOIRCS (Suzuki et al. 2003; Ichikawa et al. 2006), UKIRT/WFCAM (Casali et al. 2007), and Spitzer/IRAC (Fazio et al. 2004). The source detection on the Subaru/Scam i' -band image (Nakamura et al. 2011) and multi-band photometry are performed by using SExtractor¹ ver 2.5.0 (Bertin & Arnouts 1996). Except for the Spitzer data, the point spread function (PSF)-matched images are created by convolving the original images with Gaussian kernels to match a PSF with

full width at half maximum (FWHM) = $1.1''$. The $2.2''$ -diameter ($= 2 \times \text{PSF}$) aperture flux is measured for the PSF-matched images.

In our analysis, we use the photometry measured for the PSF-matched images of Subaru/Scam R (Hayashino et al. 2004), Subaru/Scam i' and z' (Nakamura et al. 2011), Subaru/Scam NB359 (Iwata et al. 2009), Subaru/HSC y (HSC Subaru Strategic Program Public Data Release 1; Aihara et al. 2018), and UKIRT/WFCAM K (UKIRT Infrared Deep Sky Survey Data Release 10; Lawrence et al. 2007). We list the detail of the imaging data used in this work in Table 1.

2.2 Spectroscopic targets

Our spectroscopic sample consists of 42 galaxies in the SSA22 field. Two of them are LCGs at spectroscopic redshifts ($z_{\text{spec}} \sim 3.3$) and the main targets for our MOSFIRE observation. They are selected from a sample of the LyC sources reported by Iwata et al. (2009) and Micheva et al. (2017b). In this paper, we will refer to them as LCG-1 and LCG-2. In order to observe these main targets, we set two mask fields, Mask-1 and Mask-2. 37 objects are complementary LBGs at $z_{\text{phot}} \sim 3.2 \pm 0.3$, which are selected from the SSA22HIT master catalog. We will refer to these as SSA22-LBGs in this paper. The remaining three objects are LAEs at $z_{\text{phot}} = 3.1$ (Yamada et al. 2012a,b) which are observed as filler objects (hereafter Y12LAEs). Y12LAE-2 and Y12LAE-3 are taken from the LAE candidates studied in Yamada et al. (2012a) which show significant narrow-band excess but below their criteria for the robust LAE sample. Our sample is summarized in Table 2. The details are described in the following.

2.2.1 LCG-1 and LCG-2

LCG-1 is reported by Micheva et al. (2017b) as “LBG03” in their paper. In the LyC image (Subaru/NB359 filter), two small LyC clumps are observed, separated by $\Delta r \sim 0.8''$ (see figure 2 in Micheva et al. 2017b) from the peak of the rest-frame UV continuum (Subaru/ R filter). We set the MOSFIRE slitlet on the peak of the UV continuum and use the wider slit width due to the complex morphology of LyC and UV continuum. The spectroscopic redshift is $z_{\text{spec,Ly}\alpha} = 3.287$ which is measured from the optical low-resolution spectroscopy for the Ly α emission line (Micheva et al. 2017b). Due to the blue NB359 – R color, we consider LCG-1 to be the primary high- f_{esc} candidate in our sample.

LCG-2 is also reported by Micheva et al. (2017b) as “LBG04” in their paper. The LyC image reveals a single small LyC clump, with a spatial offset of $\Delta r \sim 0.8''$ from the peak of the rest-frame UV continuum (see figure 2 in Micheva et al. 2017b). In this case, we set the slitlet to simultaneously cover the peak of the UV continuum and the LyC clump. The spectroscopic redshift is measured by Steidel et al. (2003). In Steidel et al. (2003), LCG-2 is referred to as “SSA22b-oD8” and shows $z_{\text{spec,Ly}\alpha} = 3.323$ and $z_{\text{spec,abs}} = 3.311$. According to Steidel et al. (2003), $z_{\text{spec,Ly}\alpha}$ and $z_{\text{spec,abs}}$ are measured from the Ly α emission line and the average of some absorption lines, respectively. Due to the red NB359 – R color, we consider LCG-2 to be the low- f_{esc} candidate of our sample.

2.2.2 SSA22-LBGs and Y12LAEs

The SSA22-LBGs, selected from the SSA22HIT master catalog, all have $i' < 26.4$ ($S/N > 5$) at $z_{\text{phot}} = 2.7\text{--}3.7$. We set the slitlets on the peak of the UV continuum (Subaru/ i' filter) for each

¹ <http://www.astromatic.net/software/sextractor>

Table 1. Summary of the imaging data used for our analysis.

Instrument	Filter	PSF FWHM (original, arcsec)	Limiting Mag. (smoothed, $2.2''\phi$, 5σ)	Reference
Subaru/Scam	<i>R</i>	1.08	26.5	Hayashino et al. (2004)
	<i>i'</i>	0.76	26.3	Nakamura et al. (2011)
	<i>z'</i>	0.76	25.6	Nakamura et al. (2011)
	<i>NB359</i>	0.84	26.1	Iwata et al. (2009)
Subaru/HSC	<i>y</i>	0.56	24.1	Aihara et al. (2018)
UKIRT/WFCAM	<i>K</i>	0.86	22.9	Lawrence et al. (2007)

object. The SSA22-LBGs satisfy either the color-color selection (i.e., classical Lyman break technique) or the photometric redshift estimated by using Hyperz (Bolzonella et al. 2000), or both. For our MOSFIRE observation, we first choose the SSA22-LBGs with blue UV spectral slopes β ($\beta < -2.0$) as the high-priority targets from the catalog. After that, we fix the two mask fields so as to maximize the number of high-priority targets. The remaining slitlets are set to other SSA22-LBGs. There is still a margin of slitlets which is used for the three Y12LAEs. Under the SSA22HIT project, some of the SSA22-LBGs are observed with the Deep Imaging Multi-Object Spectrograph (DEIMOS: Faber et al. 2003) mounted on the Keck-II telescope. In cases where the spectroscopic redshift has been successfully measured by the SSA22HIT project, we show the z_{spec} value in Table 2.

There are some SSA22-LBGs significantly detected in the LyC image in our sample: 11 objects display a LyC detection at the 3σ level ($NB359 < 26.7$). 6 out of the 11 objects also exhibit a blue UV slope β ($\beta < -2.0$), whereas the remaining 5 objects exhibit a red UV slope β ($\beta > -2.0$). Initially, we considered them as possible LCG candidates. However, from our MOSFIRE observations, we cannot identify any emission lines in any of these targets. Therefore, we conclude that these LBGs are not $z \sim 3$ galaxies and that the $NB359$ flux is not LyC. Hence, we do not use these object in the following analysis.

2.3 Rough estimation of LyC escape fraction

Fig. 1 shows an observed color-magnitude diagram which indicates a rough f_{esc} value and UV flux for our LCGs/SSA22-LBGs. The Subaru/ $NB359$ is a unique narrow-band filter which directly traces LyC photons from galaxies at $z \gtrsim 3.06$ (Iwata et al. 2009; Micheva et al. 2017b). Hence, the vertical axis represents the observed flux density ratio $f_{\nu, \text{UV}}/f_{\nu, \text{LyC}}$. The horizontal magenta line indicates $f_{\text{esc}} = 0.5$ assuming a set of standard parameters: IGM transmission $T_{\text{IGM}} = 0.4$ (Inoue et al. 2014), UV dust attenuation $A_{\text{UV}} = 1.67$ (Micheva et al. 2017b), and the intrinsic LyC-to-UV luminosity ratio $L_{\text{UV}}/L_{\text{LyC}} = 3$, where L is in units of $\text{erg s}^{-1} \text{Hz}^{-1}$ (e.g. Steidel et al. 2001; Inoue et al. 2005). In general, the T_{IGM} , A_{UV} , and $L_{\text{LyC}}/L_{\text{UV}}$ values change from galaxy to galaxy. These parameters should be carefully estimated by the spectral energy distribution (SED) fitting analysis (e.g. Fletcher et al. 2019). In this paper, the rough f_{esc} estimate provided by this figure will be used in an attempt to test the EW($H\beta$)- β method. However, we intend to carry out a more careful f_{esc} estimation for each object in future works by using a z_{spec} catalog for the SSA22HIT project.

As indicated by Fig. 1, LCG-1 appears to have $f_{\text{esc}} \gtrsim 0.5$, whereas LCG-2 and other SSA22-LBGs classified as sample A ($H\beta$ -detected sample) and B (redshift-confirmed sample) appear to have $f_{\text{esc}} < 0.5$. The one exception is SSA22-LBG from sample B

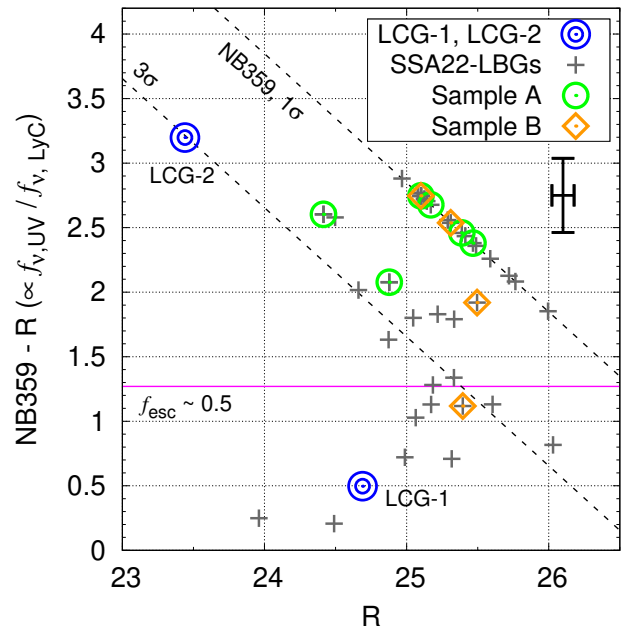


Figure 1. Observed color-magnitude diagram of $NB359 - R$ vs R . The blue double circles show our main targets, LCG-1 and LCG-2. The grey crosses denote SSA22-LBGs. The green circles and orange diamond over-plotted on the grey crosses mark the $H\beta$ -detected (sample A) and the redshift-confirmed sample (sample B), respectively, after MOSFIRE spectroscopy. The sample classification is described in Section 3.2.2. The black error-bars at top right indicate the average error of $NB359 - R$ and R . The horizontal magenta line indicates $f_{\text{esc}} \sim 0.5$ under the assumption of a set of standard parameters (see section 2.3).

(SSA22-LBG-08). While this objects seems to have $f_{\text{esc}} \sim 0.5$, the Subaru/ $NB359$ filter is contaminated by another object close to the SSA22-LBG-08. Therefore, we adopt $f_{\text{esc}} < 0.5$ for SSA22-LBG-08 as well. Some of the other SSA22-LBGs (grey crosses in Fig. 1) also show the significant detection with $NB359$ and a high f_{esc} value. However, we are unable to confirm z_{spec} of the $NB359$ -detected SSA22-LBGs due to either a single or no emission line in our MOSFIRE observation. It is therefore likely that the Subaru/ $NB359$ filter does not trace the LyC emission for these objects and we will not discuss these objects further.

Table 2. Summary of the Mask-1 and Mask-2 samples.

Name	R.A.	Dec.	z_{spec}	$NB359^a$	R^a	K^a	category ^b	Reference ^c
Mask-1								
LCG-1 ^d	22:17:08.12	00:09:58.08	3.287	25.18	24.69	23.46		(1), (2)
SSA22-LBG-01	22:17:13.56	00:07:28.93	3.087	99.00	25.17	24.19	A	(3)
SSA22-LBG-02	22:17:06.26	00:07:39.03		99.00	25.39	99.00	A	(3)
SSA22-LBG-03	22:17:09.93	00:06:02.30		99.00	25.49	24.27	C	(3)
SSA22-LBG-04	22:17:10.55	00:05:01.51		25.71	24.99	99.00	C	(3)
SSA22-LBG-05	22:17:04.73	00:06:20.91	3.112	99.00	25.59	24.55	C	(3)
SSA22-LBG-06	22:17:04.96	00:06:08.30		99.00	25.31	99.00	B	(3)
SSA22-LBG-07	22:17:04.38	00:09:20.13		24.70	24.49	23.79	C	(3)
SSA22-LBG-08	22:17:07.97	00:05:04.96		26.51	25.40	24.18	B	(3)
SSA22-LBG-09	22:17:15.33	00:04:44.39		26.96	24.88	99.00	A	(3)
SSA22-LBG-10	22:17:13.39	00:07:52.39		99.00	25.10	23.61	A	(3)
SSA22-LBG-11	22:17:09.94	00:07:19.94		99.00	25.29	24.14	C	(3)
SSA22-LBG-12	22:17:13.60	00:06:40.05		27.02	24.42	23.56	A	(3)
SSA22-LBG-13	22:17:08.65	00:06:03.99	2.869	26.51	24.87	23.92	C	(3)
SSA22-LBG-14	22:17:08.29	00:04:20.93		26.74	25.61	24.43	C	(3)
SSA22-LBG-15	22:17:13.07	00:05:46.04		99.00	25.10	99.00	C	(3)
SSA22-LBG-16	22:17:12.56	00:08:52.28		99.00	25.47	99.00	A	(3)
SSA22-LBG-17	22:17:02.60	00:08:26.93		99.00	25.10	24.17	B	(3)
SSA22-LBG-18	22:17:10.27	00:04:40.23		26.85	25.05	24.13	C	(3)
SSA22-LBG-19	22:17:04.88	00:07:51.98		27.13	25.33	99.00	C	(3)
Y12LAE-1 ^e	22:17:01.58	00:08:36.71		–	–	–	B	(4)
Y12LAE-2 ^e	22:17:03.59	00:07:09.87		–	–	–	C	(4)
Mask-2								
LCG-2 ^d	22:17:23.55	00:03:57.61	3.311	26.64	23.44	22.54		(1), (2)
SSA22-LBG-09	22:17:15.33	00:04:44.39		26.96	24.88	99.00	A	(3)
SSA22-LBG-12	22:17:13.60	00:06:40.05		27.02	24.42	23.56	A	(3)
SSA22-LBG-20	22:17:34.30	00:03:48.72		24.21	23.96	24.07	C	(3)
SSA22-LBG-21	22:17:21.76	00:05:58.43		26.30	25.17	24.11	C	(3)
SSA22-LBG-22	22:17:16.07	00:04:32.75		27.42	25.50	24.34	B	(3)
SSA22-LBG-23	22:17:29.97	00:05:10.33		27.05	25.22	24.26	C	(3)
SSA22-LBG-24	22:17:27.76	00:05:27.47		99.00	25.72	23.77	C	(3)
SSA22-LBG-25	22:17:31.10	00:06:18.31		26.85	26.03	99.00	C	(3)
SSA22-LBG-26	22:17:26.56	00:04:13.81		27.08	24.50	24.45	C	(3)
SSA22-LBG-27	22:17:25.13	00:06:14.46		99.00	25.77	99.00	C	(3)
SSA22-LBG-28	22:17:17.72	00:05:45.27		26.67	25.33	99.00	C	(3)
SSA22-LBG-29	22:17:32.95	00:04:11.91		99.00	25.14	23.16	C	(3)
SSA22-LBG-30	22:17:28.34	00:04:45.57		99.00	24.97	24.59	C	(3)
SSA22-LBG-31	22:17:14.44	00:05:00.02		26.68	24.66	23.30	C	(3)
SSA22-LBG-32	22:17:22.68	00:06:10.35	3.906	26.47	25.19	99.00	C	(3)
SSA22-LBG-33	22:17:12.47	00:06:37.72		99.00	25.13	99.00	C	(3)
SSA22-LBG-34	22:17:25.80	00:05:48.64		99.00	25.08	23.36	C	(3)
SSA22-LBG-35	22:17:18.00	00:04:09.03		99.00	25.41	99.00	C	(3)
SSA22-LBG-36	22:17:20.01	00:05:42.18		26.03	25.32	23.95	C	(3)
SSA22-LBG-37	22:17:31.91	00:04:16.57		26.09	25.06	24.10	C	(3)
Y12LAE-3	22:17:31.75	00:06:17.66		99.00	26.00	99.00	C	(4)

^a The entry 99.00 indicates a non-detection at the 1σ level.^b (A) Three, (B) two, and (C) one or no emission line are detected by our MOSFIRE observation (see Section 3.2.2).^c (1) – Iwata et al. (2009); (2) – Micheva et al. (2017b); (3) – Mawatari et al. in preparation; (4) – Yamada et al. (2012a,b).^d The $NB359$ and R -band magnitudes are same as the total magnitude shown in Micheva et al. (2017b).^e Not listed in SSA22HIT master catalog due to the non-detections in the Subaru/ i' -band.

3 MOSFIRE OBSERVATIONS

3.1 Observation and data reduction

We conduct K -band multi-object spectroscopy with the Multi-Object Spectrometer For Infra-Red Exploration (MOSFIRE; McLean et al. 2010, 2012) on the Keck-I telescope. The purpose of these observations is to determine the spectroscopic redshift using

strong emission lines such as $[\text{O III}] \lambda\lambda 4959, 5007$, and to measure the $\text{H}\beta$ emission line flux. The data was obtained on August 27, 2016 during photometric conditions with seeing $0.4''$ – $0.6''$. We applied the ABA'B' dithering pattern with a nod amplitude of $3.0''$ (A-B) and $2.4''$ (A'-B'). We mainly used slit widths of $0.7''$, which corresponds to a spectral resolution $R \sim 3600$ in the K -band, although a slit width of $0.8''$ was used for LCG-1 to cover the LyC emitting regions (see section 2.2.1).

We use two slit masks, Mask-1 and Mask-2, for our 42 LCGs/LBGs/LAEs. The field of view covered by the two slit-masks partially overlap, and SSA22-LBG-09 and SSA22-LBG-12 are observed using both slit masks. In addition to our LCGs/SSA22-LBGs targets, we also assign a slitlet on a bright and point-source like object ($K \sim 20$) in each slit mask to assess slit losses. The exposure time of Mask-1 and Mask-2 are 2.45h and 0.5h, respectively. Due to the short exposure time used for Mask-2, we fail to detect emission lines from most of the targets observe in this setting. We only use LCG-2 and SSA22-LBG-22 from Mask-2 for our following analysis.

The data reduction is performed by using the MOSFIRE data reduction pipeline (DRP)², which was developed by the MOSFIRE instrument team (Steidel et al. 2014). As a result, we obtain reduced 2-D spectra which are flat-fielded, wavelength calibrated, rectified, and sky subtracted. In the wavelength calibration procedure, we search for the best solution for each slitlet from the combination of OH night sky lines and arc lines of a neon lamp. According to Steidel et al. (2014), the wavelength of the final 2-D spectra are reduced to the vacuum wavelength and corrected for the heliocentric velocity. Therefore, we do not apply any additional correction to the reduced 2-D spectra. The 1-D spectra with their 1σ uncertainties are extracted from the reduced 2-D spectra by using the BMFP³ software developed by the MOSFIRE Deep Evolution Field team (MOSDEF; Freeman et al. 2019). For the flux calibration, we also observe a telluric standard AOV star, HIP 80974, when the star is at similar air mass as the science frames. Finally, we correct for slit losses by using the bright object in each slit mask. The total flux of the bright object is calculated from the UKIRT/K-band photometry after taking the filter response of the UKIRT/K-band into account.

We show the reduced 2-D and the extracted 1-D spectra of LCG-1 in Fig. 2 as an example. In this case, we can easily identify some emission lines, and we can extract the 1-D spectrum. In some cases, however, we are unable to identify any emission lines or the continuum from the 2-D spectrum at the object position, and hence refrain from extracting a 1-D spectrum. In Appendix, we summarize all the reduced 2-D spectra and the successfully extracted 1-D spectra.

3.2 Quick summary of MOSFIRE observations

3.2.1 LCG-1 and LCG-2

For LCG-1, we detect the three emission lines ([O III] $\lambda\lambda$ 4959, 5007 and H β), and then confirm its systemic spectroscopic redshift from [O III] λ 5007 to be $z_{\text{spec,sys}} = 3.2890$. This value is consistent with (or slightly larger than) that from the Ly α emission line inferred from optical low-resolution spectroscopy. Although the Ly α emission line may be blueshifted compared with its systemic redshift, we need the optical medium-/high-resolution spectroscopy to conclude the shift. As shown in Fig. 2, part of the H β emission line is affected by OH night sky lines. However, we judge their influence on the total line flux to be small because we are able to measure the peak of the H β emission line. Moreover, we do not find any other emission lines stemming from lower redshifts. Hence, there is no evidence that the LyC flux inferred for this target from the Subaru/NB359 image is contaminated by low- z interlopers.

For LCG-2, we detect the three emission lines ([O III] $\lambda\lambda$ 4959, 5007 and H β). The systemic redshift estimated from [O III]

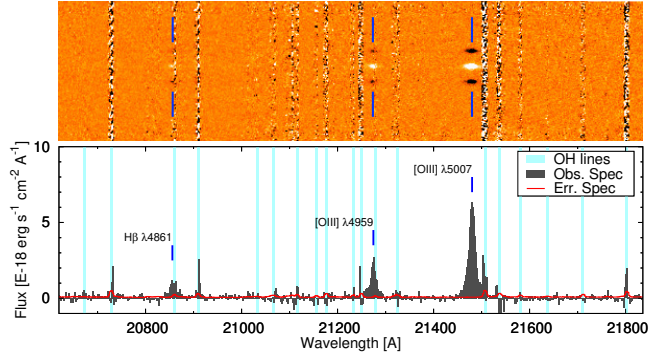


Figure 2. The reduced 2-D (top) and the extracted 1-D spectra (bottom) of LCG-1. In both panels, the identified emission lines are marked with blue thick lines. In the bottom panel, the filled dark grey histogram and the red lines represent the observed spectrum and the noise spectrum, respectively, in units of $10^{-18} \text{ erg s}^{-1} \text{ cm}^{-2} \text{ \AA}^{-1}$. The vertical cyan lines indicate the wavelengths of OH night sky lines.

λ 5007 is $z_{\text{spec,sys}} = 3.3152$, which is consistent with the redshifts reported by Steidel et al. (2003) and Micheva et al. (2017b) since $z_{\text{spec,sys}}$ typically lies somewhere between $z_{\text{spec,Ly}\alpha}$ and $z_{\text{spec,abs}}$ (e.g. Steidel et al. 2010). Since we do not find any other suspicious emission lines, there is no evidence that the LyC photons detected in the Subaru/NB359 filter stems from a low- z interloper. The bright absolute UV magnitude of LCG-2 ($M_{\text{UV}} \sim -22.0$) could potentially indicate the existence of the faint AGN in this source. In fact, the observed line width of H β is relatively large ($\text{FWHM}_{\text{raw}} \sim 300 \text{ km s}^{-1}$; Table A1). However, we do not find any other features of AGNs from our MOSFIRE observation. In order to conclude the existence of AGNs, we would need further follow-up observations such as optical spectra covering C IV λ 1549 and He II λ 1640.

3.2.2 SSA22-LBGs and Y12LAEs

For SSA22-LBGs and Y12LAEs, 1–3 emission lines are confirmed for some of the targets after visual inspection of the 2-D images and the 1-D spectrum. The detection of the three emission lines ([O III] $\lambda\lambda$ 4959, 5007 and H β) places the object in the H β -detected sample (hereafter sample “A”), whereas the detection of two emission lines places the object in the redshift-confirmed sample (hereafter sample “B”). When we detect just a single or no emission line, the object is considered part of unidentified sample (hereafter sample “C”).

After the visual inspection for SSA22-LBGs and Y12LAEs, the samples A, B, and C include 6, 5, and 29 objects, respectively. For our analysis, we use all of objects from sample A and only one object (SSA22-LBG-22) from sample B.

We here describe the details of the five objects in sample B to motivate the reason for using only SSA22-LBG-22 for our analysis. For SSA22-LBG-22, our observation significantly detects [O III] λ 5007, and marginally detects [O III] λ 4959 ($\text{S/N} \lesssim 5$) due to blending with OH night sky lines. It is in principle possible that the detection of [O III] λ 4959 is spurious and SSA22-LBG-22 is actually a lower- z object. However, the spectrum does not contain any further unidentified emission lines and the H β wavelength is not affected by the OH night sky lines. Therefore, we consider SSA22-LBG-22 as a robust member of the redshift-confirmed sample.

Three of the five objects are SSA22-LBG-06, 17, and Y12LAE-1. Their H β wavelengths are not covered by our observation due to

² <https://keck-datareductionpipelines.github.io/MosfireDRP>

³ <https://github.com/billfreeman44/bmep>

the slitlet configuration. Because we cannot obtain any information about $H\beta$, we do not use these objects. The last of the five objects is SSA22-LBG-08, for which the region covering the expected $H\beta$ wavelength is affected by OH sky lines. Due to the poor constraint on the $H\beta$ emission, we refrain from using SSA22-LBG-08 in our analysis.

4 ANALYSIS

4.1 UV spectral slope

In this work, we measure the UV spectral slope β from the photometry of Subaru/ R -, i' -, z' -, and HSC/ y -band filters by using linear least-squares fitting. According to Finkelstein et al. (2012) and Rogers et al. (2013), we apply the following function to the observed photometry,

$$m(\lambda_x) = -2.5(\beta + 2) \log \lambda_x + \text{Const} \quad (1)$$

where λ_x is the effective wavelength of x th broad-band filter, $m(\lambda_x)$ is the measured magnitude of the x th broad-band filter, and “Const” is a constant value. Our sample consists of LBGs at $z \sim 3.2 \pm 0.3$ and LAEs at $z = 3.1$. At these redshifts, the applied broad-band filters of R , i' , z' , and y in the fitting are optimal for avoiding redshifted strong spectral features such as the Ly α break ($\lambda_{\text{rest}} \sim 1216\text{\AA}$) or the Balmer break ($\lambda_{\text{rest}} \sim 3600\text{\AA}$). Our β values are listed in Table 3.

4.2 Emission line measurement

We adopt a Monte Carlo method for measuring the line profile, the total flux, and the associated uncertainties for each emission line. We first perturb the 1-D spectrum according to its 1σ noise spectrum at each pixel (hereafter referred to as a fake spectrum). We then identify the brightest emission line as [O III] λ 5007 from the fake spectrum, and estimate the spectroscopic redshift, z_{spec} , by fitting a single Gaussian profile to the line. If part of the emission line is strongly affected by the OH night sky lines, we mask the pixels in the fitting. We also calculate the total line flux by integrating the Gaussian profile. We repeat this procedure 10^4 times, and finally obtain the 10^4 measurements of the z_{spec} value, the FWHM of the line profile, and the total flux from the fake spectra. The mean and standard deviation of the distribution of the measurements are adopted as the best value and its uncertainty, respectively. By using the best z_{spec} value, we search for the redshifted emission lines of [O III] λ 4959 and $H\beta$ from each of the 10^4 fake spectra. When we identify the emission lines, we fit a single Gaussian profile, whose center is fixed based on the best z_{spec} value, to each line. In a similar way to [O III] λ 5007, we obtain the best FWHM value and the best total flux of [O III] λ 4959 and/or $H\beta$ from the 10^4 fake spectra. For the line fitting, we adopt $\lambda_{\text{rest, vac}} = 5008.240\text{\AA}$, 4960.295\AA , and 4862.683\AA , which are obtained from the Atomic Line List ver. 2.04⁴, as a vacuum wavelength of [O III] λ 5007, 4959, and $H\beta$, respectively.

As for SSA22-LBG-22 from sample B, we measure the 3σ upper-limit of the $H\beta$ emission line. On the basis of error propagation, we estimate a 1σ uncertainty in the $H\beta$ emission line flux from $\sqrt{\sum \sigma^2}$ where σ indicates the 1σ uncertainty per spectral element from the noise spectrum. For the range of the summation, we adopt

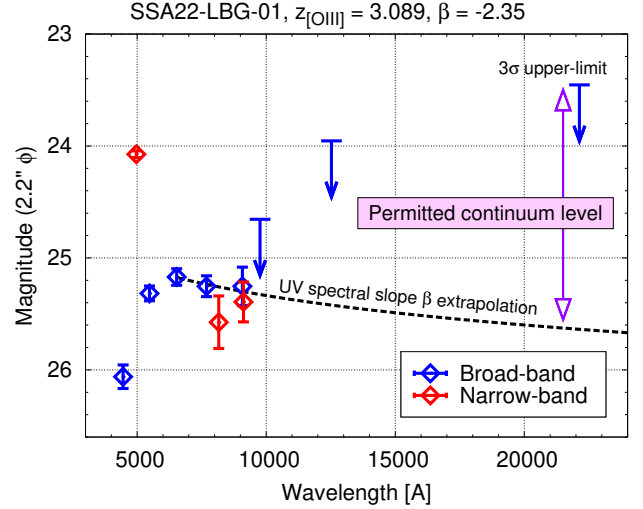


Figure 3. Illustration for estimating the permitted range of the continuum flux density. As an example, we show the spectral energy distribution of SSA22-LBG-01. The blue diamonds refer to broad-band photometry of B , V , R , i' , z' , y , J , and K from left to right. The red diamonds indicate narrow-band photometry of $NB497$, $NB816$, and $NB912$ from left to right. The black dashed line, which shows the best-fit UV spectral slope β , is extrapolated to longer wavelengths. The purple double arrow indicates the permitted range of the continuum flux density for SSA22-LBG-01.

$\lambda = \lambda_{H\beta, \text{vac}}(1+z_{\text{spec}}) \pm 3\sigma_{[\text{O III}]}$ where $\sigma_{[\text{O III}]}$ is the best standard deviation of [O III] λ 5007 calculated by $\sigma_{[\text{O III}]} = \text{FWHM}/(2\sqrt{2 \ln 2})$. In the estimation for the upper-limit, we assume that the FWHM of $H\beta$ is similar to that of [O III] λ 5007. We consider $\pm 3\sigma_{[\text{O III}]}$ to be optimal since a wider summation range results in an overestimation of the upper limit due to contamination of the OH night sky lines.

In Table 3, we show the $H\beta$ total flux for LCG-1, LCG-2, and SSA22-LBGs from which we measure the best total flux of $H\beta$. The detail results of the line measurements for our targets are described in Appendix A, and listed in Tables A1 and A2.

4.3 Equivalent width measurement

The equivalent width (EW) of $H\beta$ is obtained by $EW(H\beta) = F_{H\beta}/f_{\lambda, \text{cont}}$ where $F_{H\beta}$ is the total flux of $H\beta$ and $f_{\lambda, \text{cont}}$ is the continuum flux density at the wavelength of $H\beta$ in units of $\text{erg s}^{-1} \text{cm}^{-2} \text{\AA}^{-1}$. While we obtain $F_{H\beta}$ through our MOSFIRE observations, there are no objects detected at a significant level ($> 3\sigma$) in UKIRT/ K among the sample A and B SSA22-LBGs due to the short exposure time of K ($K_{3\sigma} \sim 23.5$). However, two SSA22-LBGs of sample A are detected at a 2σ level (SSA22-LBG-10 and SSA22-LBG-12). For LCG-1, LCG-2, and the two SSA22-LBGs, therefore, we estimate $f_{\lambda, \text{cont}}$ from the K -band photometry as an average continuum flux density around the wavelength of $H\beta$ after subtracting the contribution from the [O III] and $H\beta$ emission lines to the filter. We simply estimate the uncertainty in $EW(H\beta)$ from the uncertainty in the $H\beta$ flux and the K -band magnitude on the basis of error propagation. The measured $EW(H\beta)$ are summarized in Table 3.

For other SSA22-LBGs of sample A (and also SSA22-LBG-22), we regard them as the UKIRT/ K non-detection sample. We estimate the permitted range of the continuum flux density as follows. Fig. 3 illustrates our idea. The upper limit of the flux density

⁴ <http://www.pa.uky.edu/~peter/atomic/>

Table 3. Summary of the observed values used for the $EW(H\beta)$ – β method.

Name	z_{spec}^a	β	σ_β	$F_{H\beta}^b$ [$10^{-18} \text{ erg s}^{-1} \text{ cm}^{-2}$]	$EW_{\text{rest}}(H\beta)^c$ [Å]	f_{esc}^d
Mask-1						
LCG-1	3.2890	−2.44	0.34	19.82 ± 0.96	104.67 ± 74.53	≤ 0.7
Sample A						
SSA22-LBG-01	3.0892	−2.35	0.45	11.72 ± 0.64	[38.83 – 232.07]	0.0
SSA22-LBG-02	3.3437	−2.10	0.56	10.36 ± 0.68	[36.27 – 170.19]	0.0
SSA22-LBG-09	2.9768	−2.13	0.32	13.75 ± 1.64	[38.68 – 163.09]	0.0
SSA22-LBG-10	3.2013	−1.78	0.39	14.25 ± 0.61	55.71 ± 28.80	0.0
SSA22-LBG-12	3.1118	−2.25	0.22	27.72 ± 1.31	175.65 ± 143.71	0.0
SSA22-LBG-16	3.1041	−1.72	0.54	4.32 ± 0.58	[11.82 – 52.55]	0.0
Mask-2						
LCG-2	3.3152	−1.41	0.04	53.86 ± 3.10	86.62 ± 19.62	≤ 0.5
Sample B						
SSA22-LBG-22	3.3490	−1.64	0.57	< 2.19	< 22.33	

^a z_{spec} is estimated from the [O III] λ 5007 emission line.^b The symbol of < indicates a 3σ upper-limit.^c [XX–YY] indicates the permitted range of $EW_{\text{rest}}(H\beta)$ (see Section 4.3).^d f_{esc} is inferred from the $EW(H\beta)$ – β method.

is obtained from the 3σ limiting magnitude of the UKIRT/K-band image after correcting for the contribution of the [O III] and $H\beta$ emission lines to the filter. The lower limit of the flux density is obtained by extrapolating the UV spectral slope β from rest-frame UV to rest-frame optical wavelength. Except for special cases, the continuum flux density in the K-band will be similar to or higher than the extrapolation due to the Balmer break which is prominent for old stellar populations. In case of a strong nebular continuum with an extremely young and low-metallicity stellar population, the true continuum flux density can be lower than the extrapolation by $\Delta K \sim 0.3$ at most (e.g. Inoue 2011). Although LyC sources may have such an extreme stellar population, we believe that the extrapolation is a reasonable approximation of the lower limit on the continuum flux density. By using the upper and lower limits on the continuum flux density, we estimate the permitted range of $EW(H\beta)$ for SSA22-LBGs of sample A without the K-band detection. For SSA22-LBG-22, we estimate the upper limit of $EW(H\beta)$ from the 3σ upper limit of the $H\beta$ line flux and the lower limit of the continuum flux density. The permitted range and the upper limit on $EW(H\beta)$ are also summarized in Table 3.

5 RESULTS FROM THE $EW(H\beta)$ – β DIAGRAM

Fig. 4 shows the result of the $EW(H\beta)$ – β method to constrain f_{esc} . In this diagram, we include the data for LCG-1, LCG-2, the SSA22-LBGs of sample A, along with SSA22-LBG-22 from sample B. The blue circles filled with cyan show our main targets, LCG-1 and LCG-2. The green diamonds with error bars represent UKIRT/K-detected SSA22-LBGs of sample A (hereafter K-LBGs). The red error bars represent SSA22-LBGs of sample A, which are undetected in K at the 2σ level (hereafter nK-LBGs), whereas the horizontal error bars of the nK-LBGs represent the permitted range of $EW(H\beta)$ described in Section 4.3. The uncertainty in β is indicated by the vertical error bars. For the sake of clarity, the error bars for β are placed at the left edge of the permitted range of $EW(H\beta)$. Therefore, the red error bars denote the expected regions in which the nK-LBGs are. The orange arrow with error bars represents SSA22-LBG-22 (sample B). The

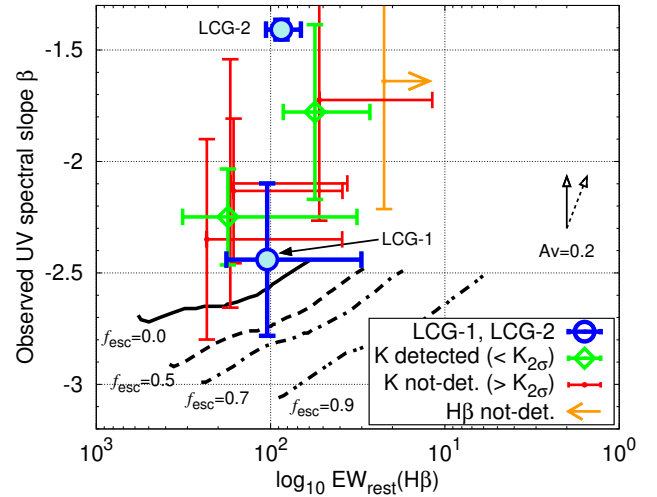


Figure 4. $EW(H\beta)$ – β diagram. The blue circles filled with cyan show our main targets, LCG-1 and LCG-2. The green diamonds show the SSA22-LBGs in sample A with marginal K-band detection at $> 2\sigma$ level (K-LBGs). The red error bars show the SSA22-LBGs in sample A which are undetected in the K-band at the 2σ level (nK-LBGs). The red error bars along with y-axis represent the permitted range of $EW(H\beta)$ estimated from the upper/lower limits on continuum flux density (see section 4.3). The orange error bar with the arrow shows the SSA22-LBG-22 (sample B) and indicates the 3σ upper limit of $EW(H\beta)$. The black solid, dashed, dot-dashed, two-dot-dashed lines show the model tracks for a radiation-bounded nebula and $Z = 0.004$ from Zackrisson et al. (2013). The two black arrows at the right hand represents the influence of the dust attenuation. For LCG-1, the f_{esc} value estimated by the $EW(H\beta)$ – β method is roughly consistent with the f_{esc} value estimated from the direct LyC measurement.

arrow denotes the upper limit on $EW(H\beta)$, estimated from the 3σ upper limit on the $H\beta$ flux and the lower limit on the continuum flux density.

In Fig. 4, we also show the model tracks for radiation-bounded

nebulae with various f_{esc} and $Z = 0.004$ from Zackrisson et al. (2013). The black solid, dashed, dot-dashed, and two-dot-dashed lines represent the models with $f_{\text{esc}} = 0.0, 0.5, 0.7$, and 0.9 , respectively. Each model track changes with the production rate of ionizing photons in a galaxy, namely, the age of the stellar population. Nebular continuum is already applied to these model tracks according to the f_{esc} values. These models are for cases without any dust attenuation ($A_V = 0.0$), even though the observed LCGs/SSA22-LBGs are affected by dust, to various degree. The impact of dust on the $\text{EW}(\text{H}\beta)$ – β diagram depends on the dust attenuation curve and geometry of dust, gas and stars in the target galaxies (Zackrisson et al. 2013, 2017). The two black arrows on the right-hand side of Fig. 4 represent two simple models for dust attenuation effects. In these simple models, we assume the Calzetti et al. (2000) attenuation curve. The black solid arrow is the case where the dust attenuation of the stellar component is the same as the attenuation of the nebular component ($A_V = A_{V,\text{neb}}$). Because the dust attenuation of the continuum and the emission line flux are the same, the arrow runs parallel to the y-axis. The black dashed arrow represents an alternative scenario where the dust attenuation of the stellar component is $0.44\times$ the dust attenuation of the nebular component ($A_V = 0.44A_{V,\text{neb}}$). The relation between A_V and $A_{V,\text{neb}}$ has been discussed by e.g. Erb et al. (2006); Kashino et al. (2013). According to these studies, the proportionality constant of the relation seems to range between 0.44 and 1.0 for high- z starbursts. Therefore, the two constant values adopted in our simple models represent reasonable assumptions.

Due to the blue UV spectral slope ($\beta \approx -2.5$) of LCG-1, we can directly compare its observed $\text{EW}(\text{H}\beta)$ and β values to the model prediction from Zackrisson et al. (2013) without considering the influence of dust attenuation. When taking the error bars in to account, we find that the $\text{EW}(\text{H}\beta)$ – β method indicates $f_{\text{esc}} = 0.0$ – 0.7 for the object LCG-1. As shown in Fig. 1, the direct LyC measurement also predicts a high f_{esc} value, $f_{\text{esc}} \gtrsim 0.5$, for this object. Hence, the two methods give broadly consistent results. It is clear, however, that given the observational uncertainties, the $\text{EW}(\text{H}\beta)$ – β method would not be able to provide useful constraints on its own, as it is only able to rule out $f_{\text{esc}} > 0.7$ for this object.

For the remaining objects, it is difficult to directly apply the $\text{EW}(\text{H}\beta)$ – β method, since their UV slopes are redder and therefore likely more affected by dust. As an example, consider LCG-2, which displays $\beta \approx -1.4$. Because the $\text{EW}(\text{H}\beta)$ value of LCG-2 formally allows $f_{\text{esc}} = 0.0$ – 0.9 , the dust-corrected (intrinsic) UV spectral slope, β_{int} , would be required for a detailed constraint on f_{esc} using the $\text{EW}(\text{H}\beta)$ – β model sequences.

In principle, the intrinsic UV slope β_{int} could potentially be derived from SED fitting, although it would be premature to attempt this at the current time. For LBGs at $z \approx 4$, the SED-fitting analysis of Yamanaka & Yamada (2019) indicates $\beta_{\text{int}} \sim -2.5 \pm 0.3$ for objects with $\beta_{\text{obs}} \sim -1.4$. Since LBGs with the same β value at $z = 3$ and $z = 4$ are, on average, expected to be similar in terms of stellar populations, one could be tempted to shift an object like LCG-2 to $\beta_{\text{int}} \sim -2.5 \pm 0.3$, in which case the $\text{EW}(\text{H}\beta)$ – β method would suggest $f_{\text{esc}} = 0.0$ – 0.5 . While this is formally consistent with the prediction from the direct LyC measurement ($f_{\text{esc}} \sim 0.0$), this would place the dust-corrected position of LCG-2 in the $\text{EW}(\text{H}\beta)$ – β diagram very close to the observed position of LCG-1, which would seem contradictory given that the direct LyC observations indicate significantly different f_{esc} for these two objects. Similar problems plague the $\text{EW}(\text{H}\beta)$ – β analysis of the other objects in Fig. 4 as well – the objects display UV slopes that are too red, and have too large

error bars, to allow conclusions on f_{esc} from their position in the $\text{EW}(\text{H}\beta)$ – β at this stage.

6 DISCUSSION

6.1 Probing the LyC escape mechanism

Throughout the paper, we have implicitly assumed f_{esc} estimated by the $\text{EW}(\text{H}\beta)$ – β method to be the same as that estimated from the direct LyC measurement. It is, however, possible that this assumption may break down in the case where the escape of LyC photons is anisotropic.

Because the direct LyC measurement depends on the optical depth of neutral hydrogen along the line-of-sight, the direct method displays a dependence on the viewing angle. The $\text{EW}(\text{H}\beta)$ – β method, on the other hand, does not have the same angular dependence. In the scenario of a ‘radiation-bounded nebula with holes’ (Zackrisson et al. 2013), also known as the picket-fence model, the LyC photons escape from the galaxy through holes or tunnels of optically thin (or almost ionized) hydrogen gas. However, the distribution of these holes and their sizes may differ across the object, and the ones facing the observer (responsible for the leakage of LyC photons detected in direct observations) may not be representative of the average across the whole galaxy. If this is the case, direct and indirect methods may not necessarily result in comparable f_{esc} estimates.

Indeed, recent observations indicate that the LyC photons from LCGs with high f_{esc} may have escaped through low-density channels of the type envisioned in the radiation-bounded nebula with holes scenario (Vanzella et al. 2016, 2018, 2019; Izotov et al. 2018b). According to Verhamme et al. (2015) and Behrens et al. (2014), a triple-peaked $\text{Ly}\alpha$ emission profile with a peak at its systemic velocity (or a double-peaked $\text{Ly}\alpha$ emission profile with a small peak separation) is predicted for high f_{esc} LCGs in this scenario, and such a spectral feature has indeed been observed in some previous works (Vanzella et al. 2018, 2019). Moreover, Rivera-Thorsen et al. (2019) report on the LyC properties and f_{esc} properties of the multiple images from the gravitationally lensed SFG at $z = 2.4$. The individual images of the LyC source in this object are spatially unresolved within the high-resolution *HST* image, which may indicate narrow escape channels.

If LyC leakage through a radiation-bounded nebula with holes is a commonly occurring phenomenon, the $\text{EW}(\text{H}\beta)$ – β method could become an important tool for probing the ‘‘angle-averaged’’ (hereafter global) escape fraction. When assessing the role of galaxies in the reionization of the Universe, it is in fact the global f_{esc} that matters, not f_{esc} in the direction of the observer (which would be measured by the direct LyC measurements).

By combining direct measurements of LyC escape (which trace optically thin holes or regions) with indirect ones (which may potentially provide a better estimate of the global f_{esc}) for the same objects, it may be possible to quantitatively assess the anisotropy of the leakage, at least in the case of SFGs at $z = 3$ – 4 and for lower-redshift analogs. It should be stressed, however, that one can only hope to detect very extreme cases of LyC leakage ($f_{\text{esc}} \gtrsim 0.5$) using the $\text{EW}(\text{H}\beta)$ – β method. Similar indirect techniques that make use of a wider set of spectroscopic data could in principle do better (Jensen et al. 2016; Giri et al. 2020).

6.2 Uncertainties in EW(H β)- β method

Here, we discuss the observational effects that dominate the uncertainties in the EW(H β)- β method, and how the errors may potentially be reduced in the future. In our analysis, the errors on EW(H β) and β are dominated by the uncertainties in the broad-band photometry at the longer wavelengths, namely, in the Subaru/ z' , y , and UKIRT/ K -band filters. Since the spectroscopic H β flux is well determined (with a typical uncertainty of $\lesssim 10\%$; Table 3), the uncertainty on EW(H β) is attributed to the large uncertainty in the continuum flux density estimated from the UKIRT/ K -band photometry.

For blue UV spectral slopes ($\beta < -2.0$), the z' - and y -band fluxes become fainter than those of the R - and i' -bands. Therefore, the uncertainty on the z' - and y -band photometry is critical for the β estimation. If we were to obtain much deeper images of z' -, y -, and K -band in the SSA22 field, the EW(H β)- β would be easier to apply.

A similar issue may also be important for attempts to apply the EW(H β)- β method to SFGs at $z > 6$. Since strong nebular emission lines are expected for SFGs at $z > 6$ (e.g. Harikane et al. 2018), emission line identification may be easily accomplished by future instruments such as *JWST*. However, if the H β continuum is undetected in the spectroscopic data, as would be expected for very faint sources and/or observations at high spectral resolution, deep imaging observations may nonetheless be important to measure the continuum flux.

The complicated effects of dust on the EW(H β)- β diagram also adds substantial uncertainty in the application of the EW(H β)- β method for estimating f_{esc} . The observational data in Fig. 4 are affected by dust, whereas the model sequences from Zackrisson et al. (2013) are for *intrinsic* EW(H β) and β prior to dust attenuation. Both the attenuation curve and the amount of dust attenuation are critical parameters in the exercise for applying the right corrections to EW(H β) and β . As mentioned in section 5, if the dust attenuation applied for the nebular component is different from that for the stellar component, the observational data points of the EW(H β)- β diagram shift diagonally from bottom left to top right as the amount of the dust attenuation is increased.

For LCG-1 (and some SSA22-LBGs), however, the observed UV spectral slope is $\beta \approx -2.5$, which is quite blue compared to the average β value of LBGs/LAEs at similar redshifts ($\beta \sim -1.7$ or -2.0 for $M_{\text{UV}} \sim -21.0$ at $z \sim 3$; e.g. Bouwens et al. 2009; Santos et al. 2019). Due to the strong dependence of β on the dust attenuation (e.g. Meurer et al. 1999), these blue UV spectral slopes β indicate that dust reddening must be small. Therefore, the observed EW(H β) and β are expected to be close to their intrinsic values, at least for LCG-1 and possibly also for some of the other SSA22-LBGs in our sample.

7 CONCLUSION

In this work, we examine the validity of the EW(H β)- β method proposed by Zackrisson et al. (2013) to indirectly estimates the escape fraction of LyC photons from individual galaxies. For this purpose, we conduct K -band multi-object spectroscopy with Keck/MOSFIRE to measure the H β emission line flux of LCGs, LBGs, and LAEs at $z \sim 3.0$ – 3.5 in the SSA22 field. Thanks to the unique Subaru/*NB359* filter, we can also directly detect the LyC flux from these objects and assess the associated escape fraction f_{esc} . Finally, we compare the outcomes of these two methods and discuss

the usefulness of combining direct and indirect methods for probing the astrophysical mechanism that allow LyC photons to escape from galaxies.

Our main conclusions can be summarized as:

(i) We reconfirm the spectroscopic redshift and measure the H β emission line flux from 2 LCGs and 6 SSA22-LBGs. The spectroscopic redshifts of our main targets, LCG-1 and LCG-2, are $z_{\text{spec}} = 3.2890$ and 3.3152 , in good agreement with the Ly α redshift values reported by Micheva et al. (2017b).

(ii) When plotting our 8 LCGs/SSA22-LBGs onto the EW(H β)- β diagram, we find LCG-1 to be suitably located for assessing f_{esc} using the Zackrisson et al. (2013) method. Based on the model predictions, we infer $f_{\text{esc}} = 0.0$ – 0.7 for this object. While this is broadly consistent with the escape fraction estimated from the directly detected LyC flux of this object ($f_{\text{esc}} \approx 0.5$), the large error bars on β and EW(H β) prevent us from setting strong quantitative constraints on the agreement. The remaining objects display UV continuum slopes β that are too red to allow any meaningful comparison without the application of dust corrections to the β slopes.

(iii) We discuss the possibility that direct and indirect LyC leakage estimates could return discrepant estimates of f_{esc} in the case of anisotropic LyC leakage, as in the case where LyC leakage happens through a radiation-bounded nebula with holes. In this scenario, the direct LyC measurements trace the covering fraction along the line of sight. This quantity may differ from the angle-averaged, “global” escape fraction that matters for the role of galaxies in the reionization of the Universe, and which could potentially be better probed through indirect f_{esc} -estimation techniques like the EW(H β)- β method. Hence, improved comparisons between these two techniques for SFGs at $z = 3$ – 4 and low- z analogs could provide useful constraints on the anisotropy of LyC leakage.

ACKNOWLEDGEMENTS

SY and AKI was supported by JSPS KAKENHI Grant Number 17H01114. TH was supported by Leading Initiative for Excellent Young Researchers, MEXT, Japan. EZ acknowledges funding from the Swedish National Space Board. The data presented herein were obtained at the W. M. Keck Observatory, which is operated as a scientific partnership among the California Institute of Technology, the University of California and the National Aeronautics and Space Administration. The Observatory was made possible by the generous financial support of the W. M. Keck Foundation. This work is based on data collected at Subaru Telescope, which is operated by the National Astronomical Observatory of Japan. The UKIDSS project is defined in Lawrence et al. (2007). UKIDSS uses the UKIRT Wide Field Camera (WFCAM; Casali et al. 2007). The photometric system is described in Hewett et al. (2006), and the calibration is described in Hodgkin et al. (2009). The pipeline processing and science archive are described in Irwin et al (2009, in prep) and Hambly et al. (2008). We use UKIDSS data release 10. Data analysis was in part carried out on the Multi-wavelength Data Analysis System operated by the Astronomy Data Center (ADC), National Astronomical Observatory of Japan. The authors wish to recognize and acknowledge the very significant cultural role and reverence that the summit of Maunakea has always had within the indigenous Hawaiian community. We are most fortunate to have the opportunity to conduct observations from this mountain.

REFERENCES

- Aihara H., et al., 2018, *PASJ*, **70**, S8
- Behrens C., Dijkstra M., Niemeyer J. C., 2014, *A&A*, **563**, A77
- Bergvall N., Zackrisson E., Andersson B. G., Arnberg D., Masegosa J., Östlin G., 2006, *A&A*, **448**, 513
- Bertin E., Arnouts S., 1996, *A&AS*, **117**, 393
- Bian F., Fan X., McGreer I., Cai Z., Jiang L., 2017, *ApJ*, **837**, L12
- Bolzonella M., Miralles J. M., Pelló R., 2000, *A&A*, **363**, 476
- Borthakur S., Heckman T. M., Leitherer C., Overzier R. A., 2014, *Science*, **346**, 216
- Boulade O., et al., 2003, MegaCam: the new Canada-France-Hawaii Telescope wide-field imaging camera. pp 72–81, doi:10.1117/12.459890
- Bouwens R. J., et al., 2009, *ApJ*, **705**, 936
- Bouwens R. J., et al., 2014, *ApJ*, **793**, 115
- Bouwens R. J., Smit R., Labbé I., Franx M., Caruana J., Oesch P., Stefanon M., Rasappu N., 2016, *ApJ*, **831**, 176
- Calzetti D., Kinney A. L., Storchi-Bergmann T., 1994, *ApJ*, **429**, 582
- Calzetti D., Armus L., Bohlin R. C., Kinney A. L., Koornneef J., Storchi-Bergmann T., 2000, *ApJ*, **533**, 682
- Casali M., et al., 2007, *A&A*, **467**, 777
- Dijkstra M., Gronke M., Venkatesan A., 2016, *ApJ*, **828**, 71
- Erb D. K., Steidel C. C., Shapley A. E., Pettini M., Reddy N. A., Adelberger K. L., 2006, *ApJ*, **647**, 128
- Faber S. M., et al., 2003, The DEIMOS spectrograph for the Keck II Telescope: integration and testing. pp 1657–1669, doi:10.1117/12.460346
- Fan X., Narayanan V. K., Strauss M. A., White R. L., Becker R. H., Pentericci L., Rix H.-W., 2002, *AJ*, **123**, 1247
- Fan X., et al., 2006, *AJ*, **132**, 117
- Fazio G. G., et al., 2004, *ApJS*, **154**, 10
- Finkelstein S. L., et al., 2012, *ApJ*, **756**, 164
- Finkelstein S. L., et al., 2015, *ApJ*, **810**, 71
- Finkelstein S. L., et al., 2019, *ApJ*, **879**, 36
- Fletcher T. J., Tang M., Robertson B. E., Nakajima K., Ellis R. S., Stark D. P., Inoue A., 2019, *ApJ*, **878**, 87
- Freeman W. R., et al., 2019, *ApJ*, **873**, 102
- Fukugita M., Ichikawa T., Gunn J. E., Doi M., Shimasaku K., Schneider D. P., 1996, *AJ*, **111**, 1748
- Giri S. K., Zackrisson E., Binggeli C., Pelckmans K., Cubo R., 2020, *MNRAS*, **491**, 5277
- Grazian A., et al., 2016, *A&A*, **585**, A48
- Greiner J., et al., 2009, *ApJ*, **693**, 1610
- Hambly N. C., et al., 2008, *MNRAS*, **384**, 637
- Harikane Y., et al., 2018, *ApJ*, **859**, 84
- Hayashino T., et al., 2004, *AJ*, **128**, 2073
- Hewett P. C., Warren S. J., Leggett S. K., Hodgkin S. T., 2006, *MNRAS*, **367**, 454
- Hodgkin S. T., Irwin M. J., Hewett P. C., Warren S. J., 2009, *MNRAS*, **394**, 675
- Ichikawa T., et al., 2006, MOIRCS: multi-object infrared camera and spectrograph for SUBARU. p. 626916, doi:10.1117/12.670078
- Inoue A. K., 2011, *MNRAS*, **415**, 2920
- Inoue A. K., Iwata I., 2008, *MNRAS*, **387**, 1681
- Inoue A. K., Iwata I., Deharveng J. M., Buat V., Burgarella D., 2005, *A&A*, **435**, 471
- Inoue A. K., Iwata I., Deharveng J.-M., 2006, *MNRAS*, **371**, L1
- Inoue A. K., Shimizu I., Iwata I., Tanaka M., 2014, *MNRAS*, **442**, 1805
- Itoh R., et al., 2018, *ApJ*, **867**, 46
- Iwata I., et al., 2009, *ApJ*, **692**, 1287
- Iwata I., Inoue A. K., Micheva G., Matsuda Y., Yamada T., 2019, *MNRAS*, **488**, 5671
- Izotov Y. I., Schaerer D., Thuan T. X., Worseck G., Guseva N. G., Orlitová I., Verhamme A., 2016a, *MNRAS*, **461**, 3683
- Izotov Y. I., Orlitová I., Schaerer D., Thuan T. X., Verhamme A., Guseva N. G., Worseck G., 2016b, *Nature*, **529**, 178
- Izotov Y. I., Schaerer D., Worseck G., Guseva N. G., Thuan T. X., Verhamme A., Orlitová I., Fricke K. J., 2018a, *MNRAS*, **474**, 4514
- Izotov Y. I., Worseck G., Schaerer D., Guseva N. G., Thuan T. X., Fricke Verhamme A., Orlitová I., 2018b, *MNRAS*, **478**, 4851
- Jensen H., Zackrisson E., Pelckmans K., Binggeli C., Ausmees K., Lundholm U., 2016, *ApJ*, **827**, 5
- Kashikawa N., et al., 2006, *ApJ*, **648**, 7
- Kashikawa N., et al., 2011, *ApJ*, **734**, 119
- Kashino D., et al., 2013, *ApJ*, **777**, L8
- Konno A., et al., 2018, *PASJ*, **70**, S16
- Kulkarni G., Worseck G., Hennawi J. F., 2019, *MNRAS*, **488**, 1035
- Lawrence A., et al., 2007, *MNRAS*, **379**, 1599
- Lee K.-G., et al., 2014, *ApJ*, **795**, L12
- Lee K.-G., et al., 2018, *ApJS*, **237**, 31
- Leitet E., Bergvall N., Piskunov N., Andersson B. G., 2011, *A&A*, **532**, A107
- Leitet E., Bergvall N., Hayes M., Linné S., Zackrisson E., 2013, *A&A*, **553**, A106
- Madau P., Haardt F., 2015, *ApJ*, **813**, L8
- Madau P., Haardt F., Rees M. J., 1999, *ApJ*, **514**, 648
- Matsuoka Y., et al., 2018, *ApJ*, **869**, 150
- McLean I. S., et al., 2010, Design and development of MOSFIRE: the multi-object spectrometer for infrared exploration at the Keck Observatory. p. 77351E, doi:10.1117/12.856715
- McLean I. S., et al., 2012, MOSFIRE, the multi-object spectrometer for infra-red exploration at the Keck Observatory. p. 84460J, doi:10.1117/12.924794
- Meurer G. R., Heckman T. M., Calzetti D., 1999, *ApJ*, **521**, 64
- Micheva G., Iwata I., Inoue A. K., 2017a, *MNRAS*, **465**, 302
- Micheva G., Iwata I., Inoue A. K., Matsuda Y., Yamada T., Hayashino T., 2017b, *MNRAS*, **465**, 316
- Miyazaki S., et al., 2002, *PASJ*, **54**, 833
- Miyazaki S., et al., 2012, Hyper Suprime-Cam. p. 84460Z, doi:10.1117/12.926844
- Miyazaki S., et al., 2018, *PASJ*, **70**, S1
- Mostardi R. E., Shapley A. E., Nestor D. B., Steidel C. C., Reddy N. A., Trainor R. F., 2013, *ApJ*, **779**, 65
- Mostardi R. E., Shapley A. E., Steidel C. C., Trainor R. F., Reddy N. A., Siana B., 2015, *ApJ*, **810**, 107
- Naidu R. P., et al., 2017, *ApJ*, **847**, 12
- Nakajima K., Ouchi M., 2014, *MNRAS*, **442**, 900
- Nakajima K., Ouchi M., Shimasaku K., Hashimoto T., Ono Y., Lee J. C., 2013, *ApJ*, **769**, 3
- Nakajima K., Ellis R. S., Robertson B. E., Tang M., Stark D. P., 2019, arXiv e-prints, p. arXiv:1909.07396
- Nakamura E., Inoue A. K., Hayashino T., Horie M., Kousai K., Fujii T., Matsuda Y., 2011, *MNRAS*, **412**, 2579
- Nestor D. B., Shapley A. E., Steidel C. C., Siana B., 2011, *ApJ*, **736**, 18
- Nestor D. B., Shapley A. E., Kornei K. A., Steidel C. C., Siana B., 2013, *ApJ*, **765**, 47
- Oke J. B., Gunn J. E., 1983, *ApJ*, **266**, 713
- Ono Y., et al., 2012, *ApJ*, **744**, 83
- Ouchi M., et al., 2010, *ApJ*, **723**, 869
- Ouchi M., et al., 2018, *PASJ*, **70**, S13
- Paardekooper J.-P., Khochfar S., Dalla Vecchia C., 2015, *MNRAS*, **451**, 2544
- Planck Collaboration et al., 2016, *A&A*, **596**, A108
- Rivera-Thorsen T. E., et al., 2019, *Science*, **366**, 738
- Robertson B. E., Ellis R. S., Furlanetto S. R., Dunlop J. S., 2015, *ApJ*, **802**, L19
- Rogers A. B., McLure R. J., Dunlop J. S., 2013, *MNRAS*, **429**, 2456
- Santos S., et al., 2019, arXiv e-prints, p. arXiv:1910.02959
- Schenker M. A., Stark D. P., Ellis R. S., Robertson B. E., Dunlop J. S., McLure R. J., Kneib J.-P., Richard J., 2012, *ApJ*, **744**, 179
- Shapley A. E., Steidel C. C., Strom A. L., Bogosavljević M., Reddy N. A., Siana B., Mostardi R. E., Rudie G. C., 2016, *ApJ*, **826**, L24
- Siana B., et al., 2007, *ApJ*, **668**, 62
- Siana B., et al., 2010, *ApJ*, **723**, 241
- Siana B., et al., 2015, *ApJ*, **804**, 17
- Steidel C. C., Pettini M., Adelberger K. L., 2001, *ApJ*, **546**, 665

- Steidel C. C., Adelberger K. L., Shapley A. E., Pettini M., Dickinson M., Giavalisco M., 2003, *ApJ*, **592**, 728
- Steidel C. C., Erb D. K., Shapley A. E., Pettini M., Reddy N., Bogosavljević M., Rudie G. C., Rakic O., 2010, *ApJ*, **717**, 289
- Steidel C. C., et al., 2014, *ApJ*, **795**, 165
- Steidel C. C., Bogosavljević M., Shapley A. E., Reddy N. A., Rudie G. C., Pettini M., Trainor R. F., Strom A. L., 2018, *ApJ*, **869**, 123
- Suzuki R., Tokoku C., Ichikawa T., Nishimura T., 2003, Optical design of MOIRCS. pp 307–318, doi:10.1117/12.461446
- Tanvir N. R., et al., 2019, *MNRAS*, **483**, 5380
- Totani T., Kawai N., Kosugi G., Aoki K., Yamada T., Iye M., Ohta K., Hattori T., 2006, *PASJ*, **58**, 485
- Totani T., Aoki K., Hattori T., Kawai N., 2016, *PASJ*, **68**, 15
- Vanzella E., Siana B., Cristiani S., Nonino M., 2010a, *MNRAS*, **404**, 1672
- Vanzella E., et al., 2010b, *ApJ*, **725**, 1011
- Vanzella E., et al., 2016, *ApJ*, **825**, 41
- Vanzella E., et al., 2018, *MNRAS*, **476**, L15
- Vanzella E., et al., 2019, *MNRAS*, p. 2218
- Vasei K., et al., 2016, *ApJ*, **831**, 38
- Verhamme A., Orlitová I., Schaerer D., Hayes M., 2015, *A&A*, **578**, A7
- Verhamme A., Orlitová I., Schaerer D., Izotov Y., Wörzner G., Thuan T. X., Guseva N., 2017, *A&A*, **597**, A13
- Wilkins S. M., Bunker A., Coulton W., Croft R., di Matteo T., Khandai N., Feng Y., 2013, *MNRAS*, **430**, 2885
- Wise J. H., Demchenko V. G., Halicek M. T., Norman M. L., Turk M. J., Abel T., Smith B. D., 2014, *MNRAS*, **442**, 2560
- Yajima H., Choi J.-H., Nagamine K., 2011, *MNRAS*, **412**, 411
- Yamada T., Nakamura Y., Matsuda Y., Hayashino T., Yamauchi R., Morimoto N., Kousai K., Umemura M., 2012a, *AJ*, **143**, 79
- Yamada T., Matsuda Y., Kousai K., Hayashino T., Morimoto N., Umemura M., 2012b, *ApJ*, **751**, 29
- Yamanaka S., Yamada T., 2019, *PASJ*, **71**, 51
- Zackrisson E., Inoue A. K., Jensen H., 2013, *ApJ*, **777**, 39
- Zackrisson E., et al., 2017, *ApJ*, **836**, 78
- Zahn O., et al., 2012, *ApJ*, **756**, 65
- de Barros S., et al., 2016, *A&A*, **585**, A51

at $z_{\text{phot}} = 3.1$ studied in Yamada et al. (2012a), although the narrow-band excess was below their criteria for the robust LAE sample. If assuming the single emission line detected by our MOSFIRE observation is [O III] $\lambda 5007$, the spectroscopic redshift is $z_{\text{spec}, [\text{O III}]} = 3.1147$. Since the spectroscopic redshift is consistent with the photometric redshift, Y12LAE-3 is a new redshift-confirmed object by our observation. However, the $H\beta$ wavelength is not covered by our observation due to the MOSFIRE slitlet configuration. Therefore, this object is not used for our analysis.

APPENDIX A: REDUCED 2-D IMAGES AND 1-D SPECTRA OF ALL OUR TARGETS

We here show all the reduced 2-D spectra image and the successfully extracted 1-D spectra in Fig. A1. In cases where the 1-D spectrum is not extracted, we only show the 2-D spectral image. In Tables A1 and A2, we show the results of the flux measurements. The following is brief comments on some sample C objects, i.e. SSA22-LBG-05, SSA22-LBG-13, and Y12LAE-3.

SSA22-LBG-05. This object is observed by Keck/DEIMOS under the SSA22HIT project. The spectroscopic redshift is $z_{\text{spec}, \text{Ly}\alpha} = 3.112$ which is measured from the DEIMOS observation for the $\text{Ly}\alpha$ emission line. If assuming the single emission line detected by our MOSFIRE observation is [O III] $\lambda 5007$, the spectroscopic redshift is $z_{\text{spec}, [\text{O III}]} = 3.1154$. Since the spectroscopic redshift is consistent in the observations, SSA22-LBG-05 is actually a redshift-confirmed object. However, the $H\beta$ wavelength is not covered by our observation due to the MOSFIRE slitlet configuration. Therefore, this object is not used for our analysis.

SSA22-LBG-13. This object is observed by Keck/DEIMOS under the SSA22HIT project. The spectroscopic redshift is $z_{\text{spec}, \text{Ly}\alpha} = 2.869$. If assuming the single emission line detected by our MOSFIRE observation is [O III] $\lambda 5007$ or $H\alpha$ ($\lambda_{\text{vac}} = 6564.61$), the spectroscopic redshift is $z_{\text{spec}, [\text{O III}]} = 3.7322$ or $z_{\text{spec}, H\alpha} = 2.6103$, respectively. The spectroscopic redshift is not consistent in the observations. Therefore, this object is still a unidentified object.

Y12LAE-3. This object is taken from the LAE candidates

Table A1. Summary of flux measurement for LCG-1, LCG-2, and the SSA22-LBGs classified as belonging to sample A and B.

Name	z_{spec}^a	λ^b	[O III] $\lambda 5007$ FWHM ^c	Total Flux ^d	$\lambda^{a,e}$	[O III] $\lambda 4959$ FWHM ^c	Total Flux ^d	$\lambda^{a,e}$	H β ^f FWHM ^c	Total Flux ^d
Mask-1										
LCG-1	3.2890	21480.1	248.0	112.57 \pm 0.77	21274.5	233.9	38.05 \pm 0.87	20855.8	282.7	19.82 \pm 0.96
Sample A										
SSA22-LBG-01	3.0892	20479.9	145.1	72.91 \pm 0.68	20283.9	155.1	23.99 \pm 1.11	19884.7	161.8	11.72 \pm 0.64
SSA22-LBG-02	3.3437	21754.0	205.7	60.36 \pm 0.86	21545.8	245.5	21.77 \pm 1.13	21121.8	211.4	10.36 \pm 0.68
SSA22-LBG-09	2.9768	19916.5	179.8	121.30 \pm 0.96	19725.9	184.0	40.07 \pm 0.99	19337.7	276.3	13.75 \pm 1.64
SSA22-LBG-10	3.2013	21040.9	214.2	44.14 \pm 1.08	20839.4	223.6	16.68 \pm 0.85	20429.3	188.8	14.25 \pm 0.61
SSA22-LBG-12	3.1118	20592.8	172.3	171.40 \pm 0.88	20395.7	171.1	58.25 \pm 0.68	19994.3	166.4	27.72 \pm 1.31
SSA22-LBG-16	3.1041	20554.2	105.1	13.24 \pm 1.16	20357.5	167.1	4.42 \pm 0.42	19956.8	156.7	4.32 \pm 0.58
Sample B										
SSA22-LBG-06	3.1098	20583.0	144.7	15.78 \pm 1.24	20386.0	182.6	5.24 \pm 0.51	19984.8	–	–
SSA22-LBG-08	3.3327	21699.3	131.6	22.34 \pm 0.64	21491.6	112.5	6.26 \pm 0.45	21068.6	-99	-99
SSA22-LBG-17	3.0734	20400.3	166.3	51.37 \pm 0.75	20205.0	186.9	18.78 \pm 1.10	19807.4	–	–
Y12LAE-1	3.0824	20445.6	100.9	8.14 \pm 0.38	20249.8	173.7	4.56 \pm 0.56	19851.3	–	–
Mask-2										
LCG-2	3.3152	21611.3	309.5	140.57 \pm 3.11	21404.4	335.4	54.60 \pm 4.41	20983.2	340.9	53.86 \pm 3.10
Sample A										
SSA22-LBG-09	2.9772	19918.7	178.8	117.95 \pm 2.40	19728.0	201.8	39.83 \pm 3.05	19339.8	–	–
SSA22-LBG-12	3.1116	20591.9	210.4	136.47 \pm 2.19	20394.8	118.1	26.19 \pm 1.05	19993.5	–	–
Sample B										
SSA22-LBG-22	3.3490	21780.9	122.2	16.37 \pm 1.24	21572.4	113.2	6.86 \pm 1.44	21147.9		< 2.19

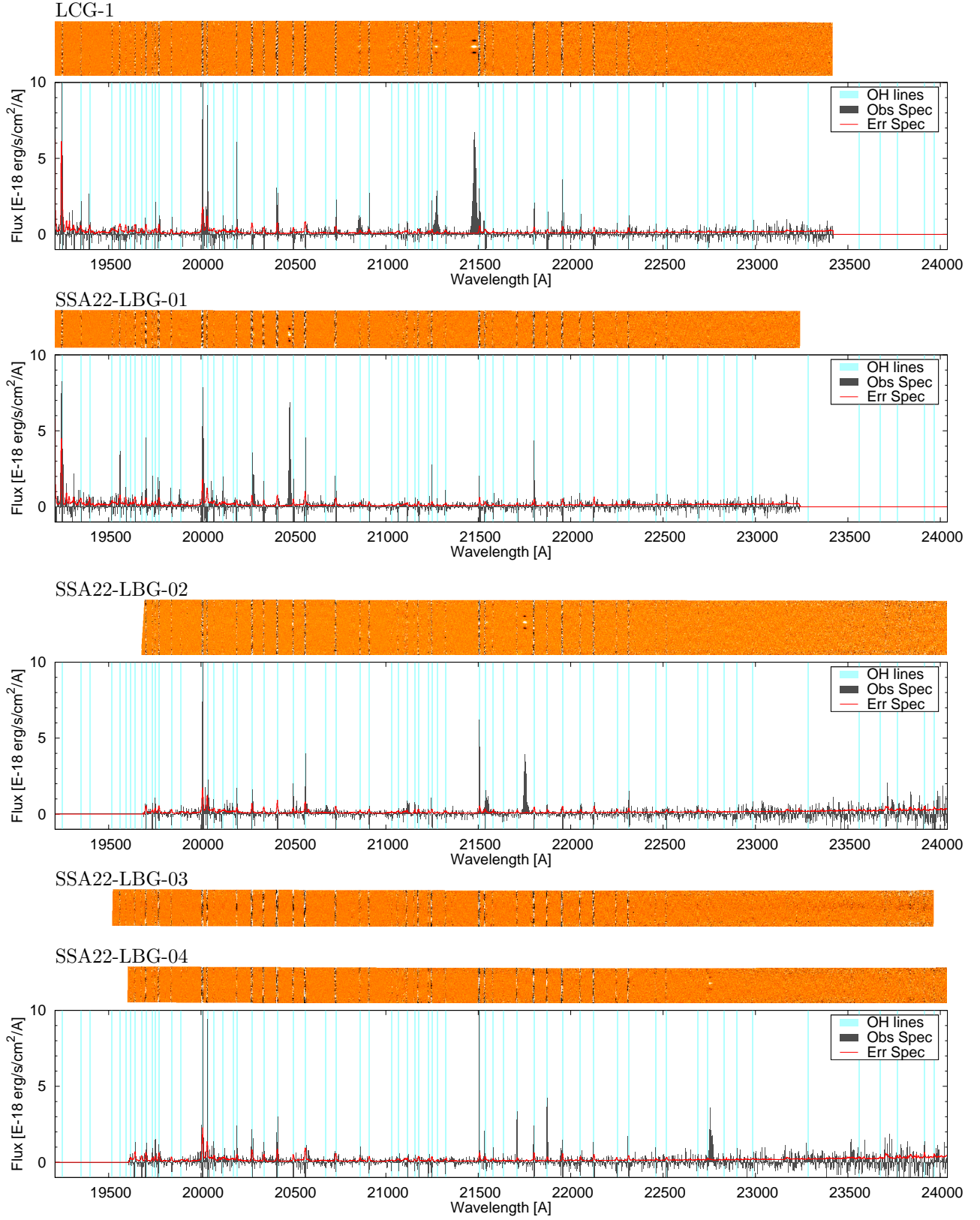
^a z_{spec} is estimated from the [O III] $\lambda 5007$ emission line.^b Center of Gaussian function in units of Å.^c FWHM of Gaussian function in units of km s^{-1} . FWHM is not corrected for the instrumental broadening.^d Total flux in units of $10^{-18} \text{ erg s}^{-1} \text{ cm}^{-2}$.^e The center wavelength of [O III] $\lambda 4959$ and $\text{H}\beta$ are calculated from z_{spec} and their vacuum wavelength. They are fixed in the flux measurement.^f “–” indicates that the predicted wavelength is the outside of the wavelength coverage of our MOSFIRE observation.

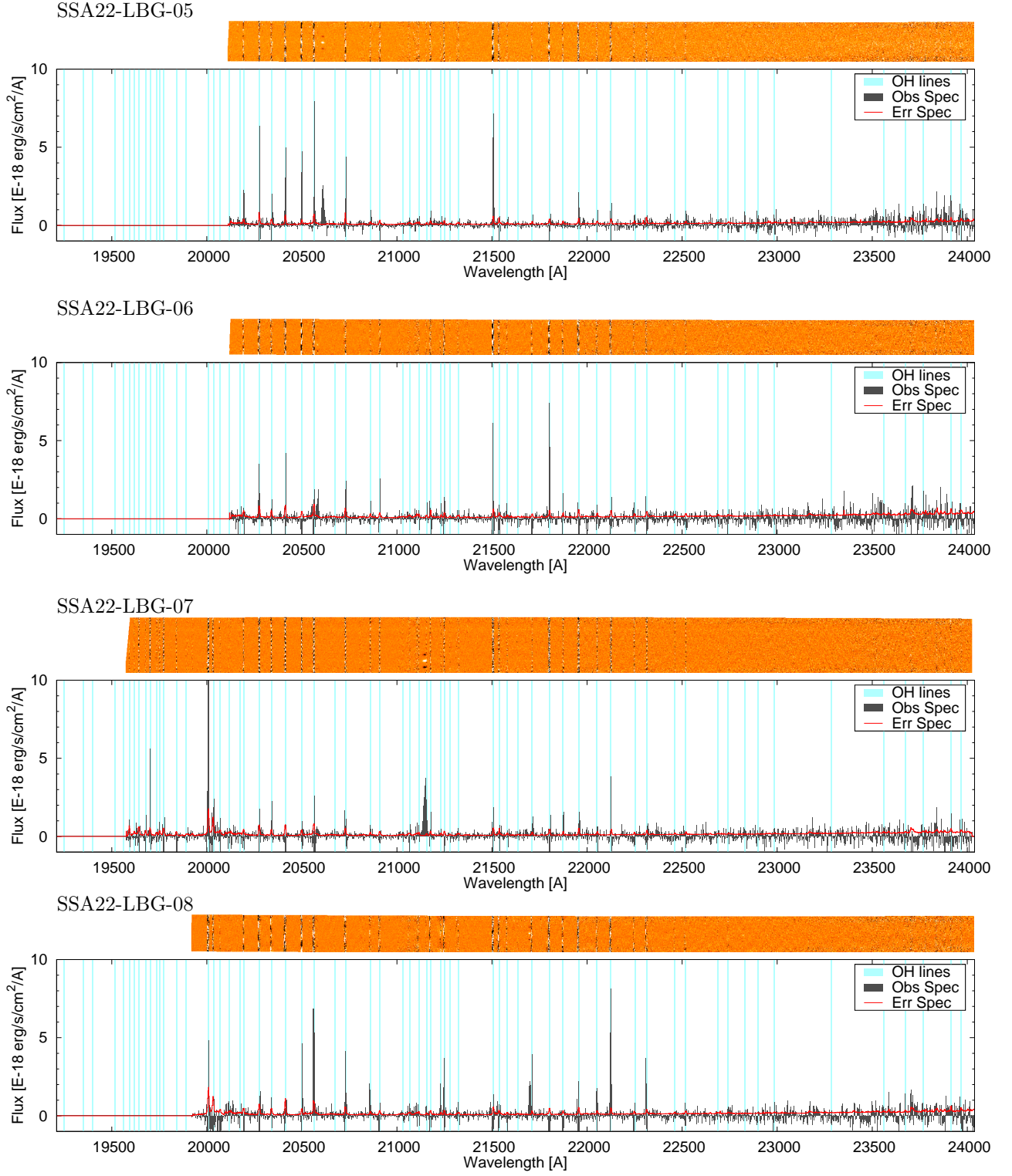
“–99” indicates that the predicted wavelength is strongly affected by OH night sky lines.

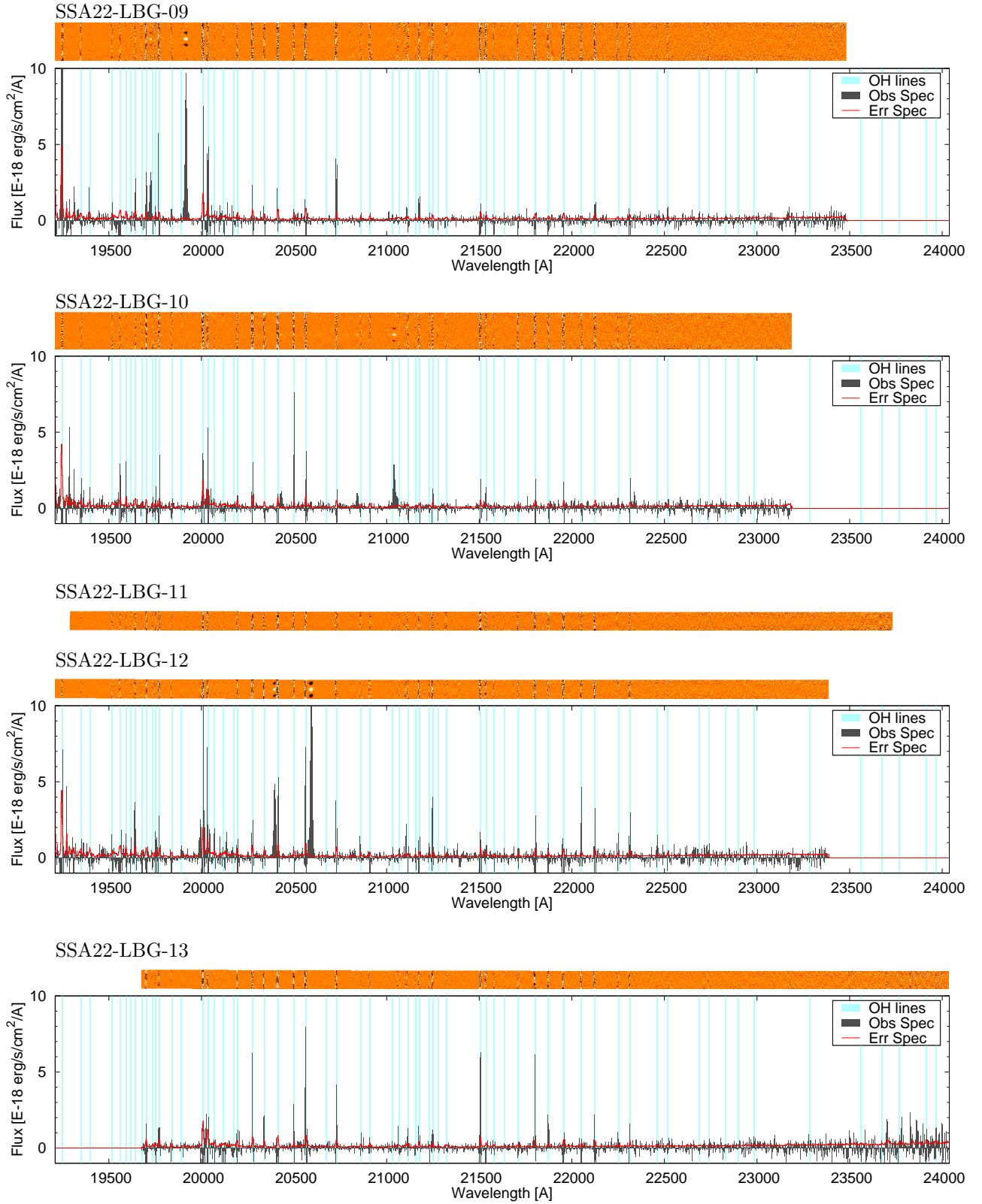
Table A2. Summary of flux measurement for SSA22-LBGs classified as belonging to sample C.

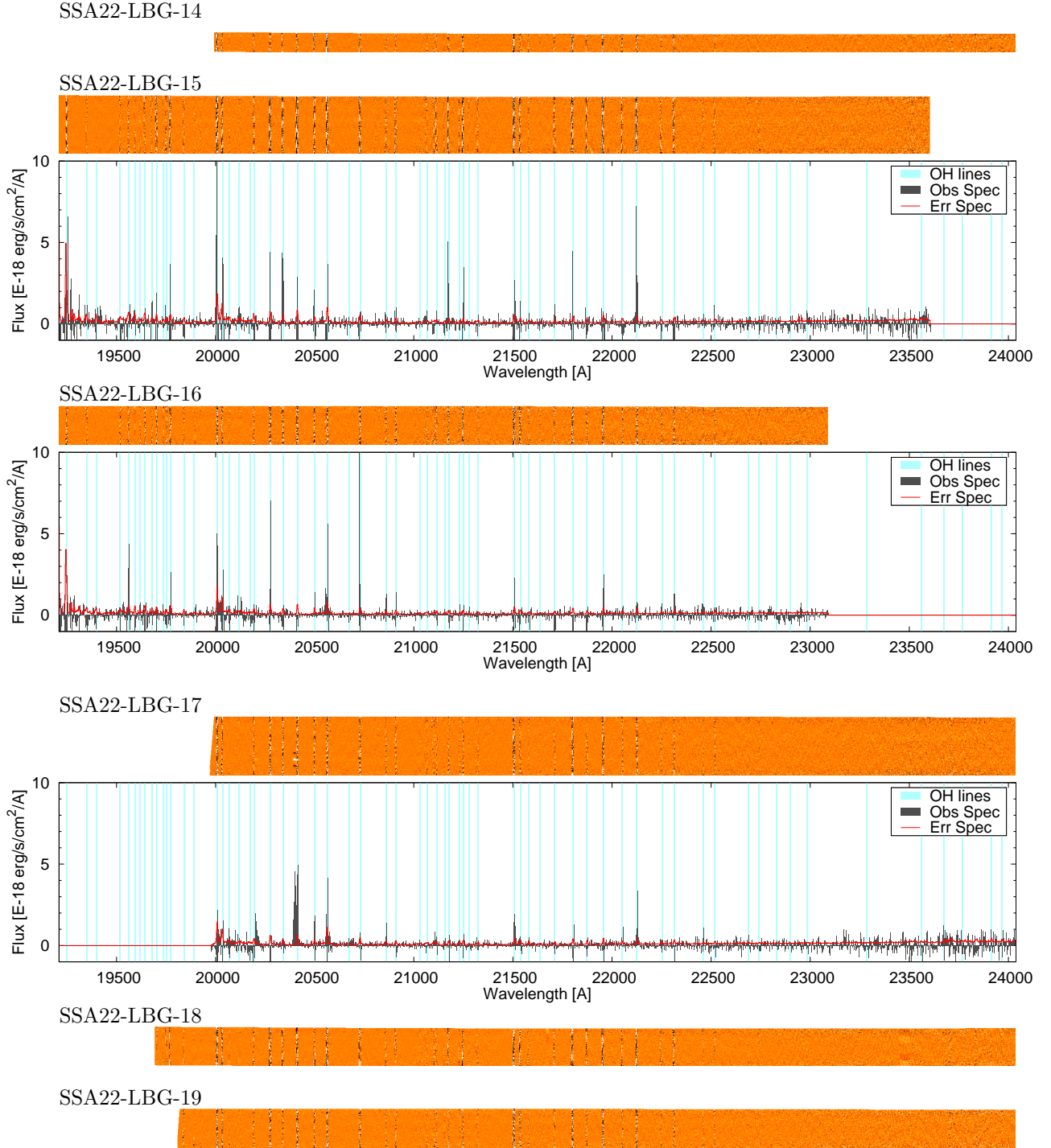
Name	Unidentified emission line		Comment	
	λ^a	FWHM ^b	Total Flux ^c	
Mask-1				
SSA22-LBG-04	22757.1	195.7	45.37 ± 1.69	Line profile looks like [O II] $\lambda\lambda 3726, 3729$ doublet.
SSA22-LBG-05	20611.2	182.5	32.32 ± 0.54	Observed by Keck/DEIMOS under SSA22HIT project.
SSA22-LBG-07	21148.2	235.9	59.75 ± 0.79	
SSA22-LBG-13	23700.2	122.3	11.64 ± 1.99	Observed by Keck/DEIMOS under SSA22HIT project.
SSA22-LBG-15	19414.4	281.1	15.09 ± 1.73	
Mask-2				
SSA22-LBG-26	19370.5	201.1	52.54 ± 3.21	
SSA22-LBG-31	21693.0	159.2	27.70 ± 1.93	
Y12LAE-3	20607.5	174.9	21.39 ± 1.15	Suppose line is [O III] $\lambda 5007$, z_{spec} is consistent with z_{phot} of Y12LAEs.

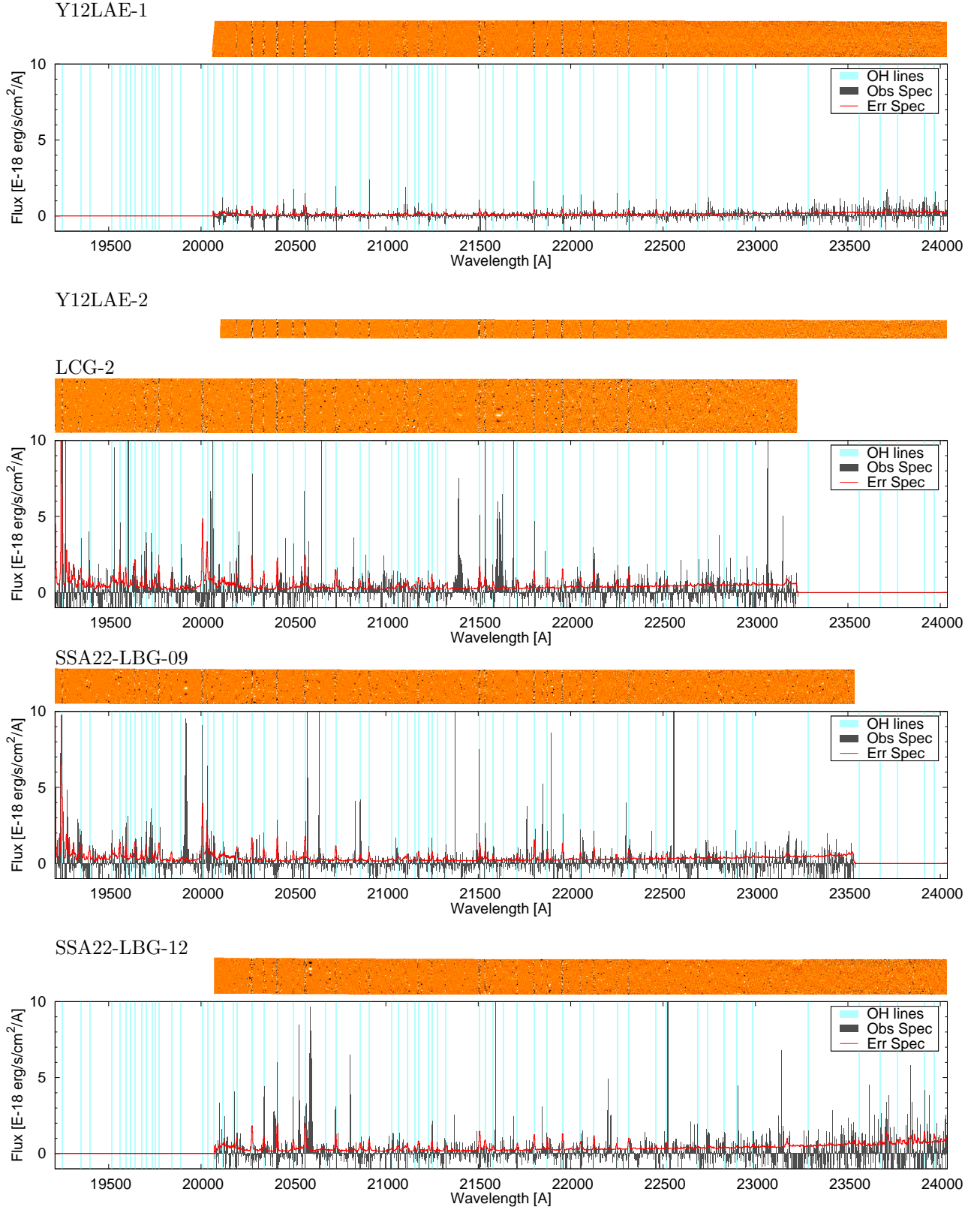
^a Center of Gaussian function in units of Å.^b FWHM of Gaussian function in units of km s^{-1} . FWHM is not corrected for the instrumental broadening.^c Total flux in units of $10^{-18} \text{ erg s}^{-1} \text{ cm}^{-2}$.This paper has been typeset from a \LaTeX file prepared by the author.

**Figure A1.** Reduced 2-D images and 1-D spectra.

Figure A1 – *continued* Reduced 2-D images and 1-D spectra.

**Figure A1** – *continued* Reduced 2-D images and 1-D spectra.

Figure A1 – *continued* Reduced 2-D images and 1-D spectra.

**Figure A1** – *continued* Reduced 2-D images and 1-D spectra.

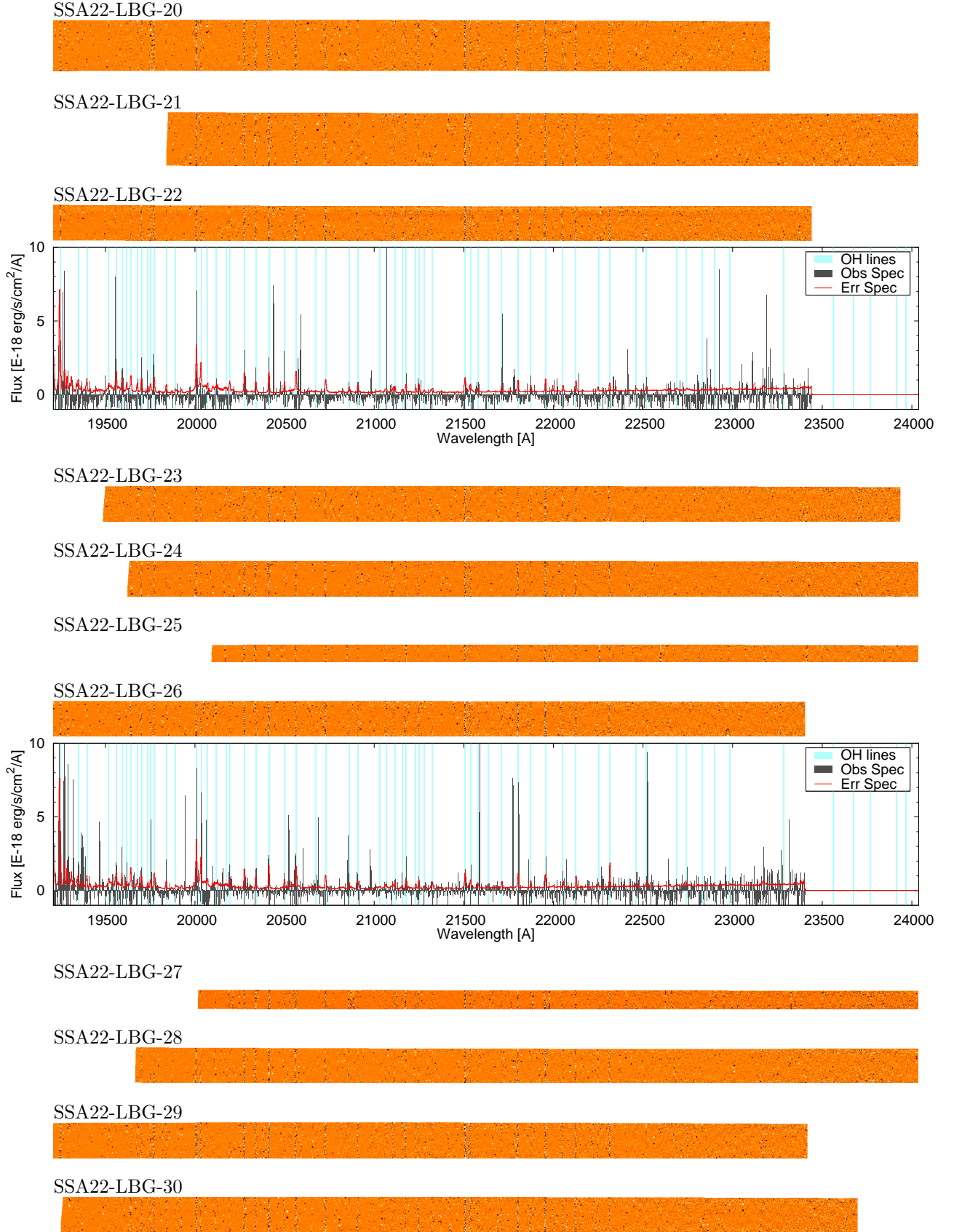


Figure A1 – continued Reduced 2-D images and 1-D spectra.

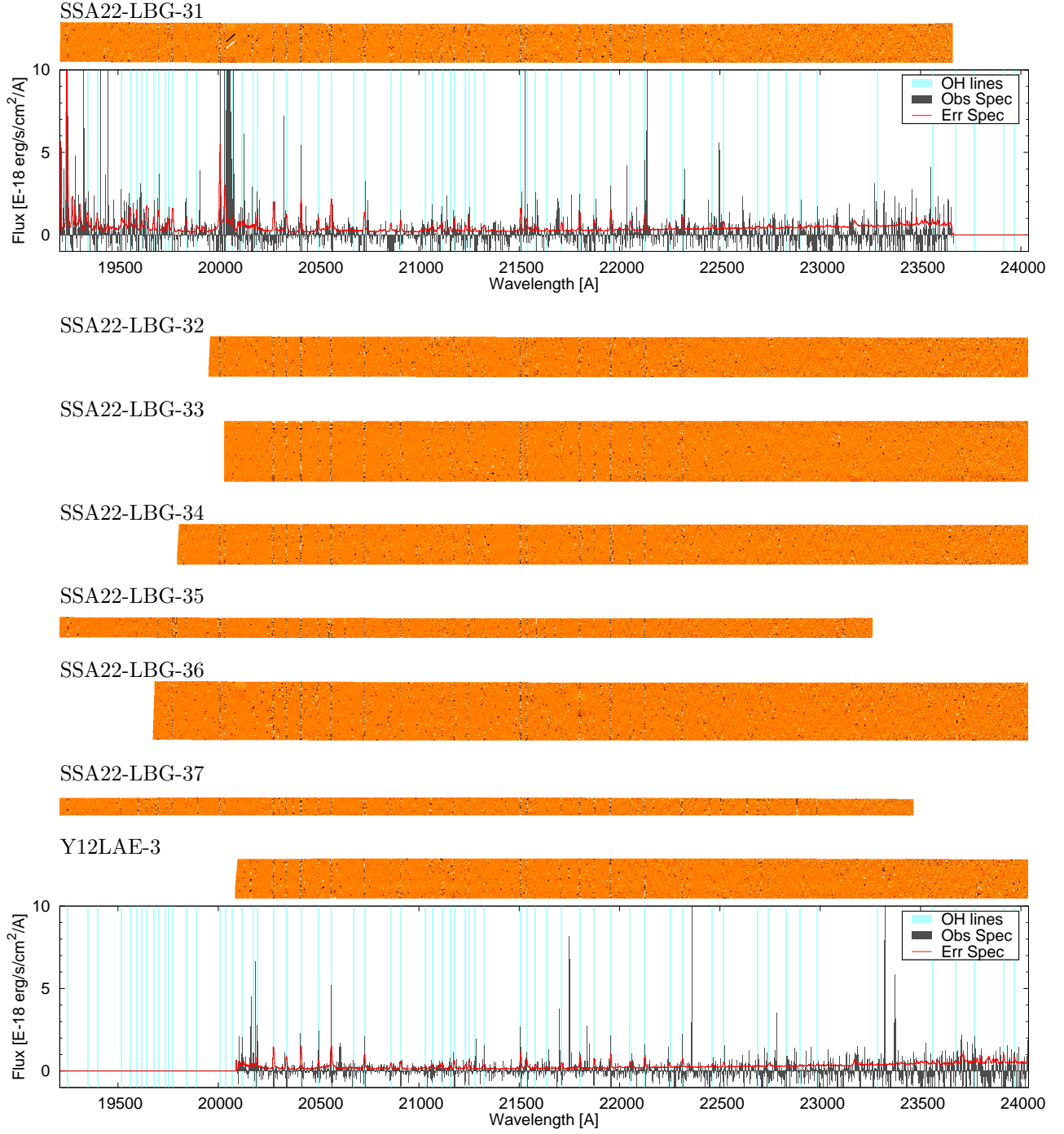


Figure A1 – *continued* Reduced 2-D images and 1-D spectra.